MATERIALS CHEMISTRY
FRONTIERS

REVIEW

View Article Online
View Journal | View Issue

Cite this: *Mater. Chem. Front.*, 2017, **1**, 2155

Recent advances in metal–nitrogen–carbon catalysts for electrochemical water splitting

Kaihua Liu,[ab] Haixia Zhong,[a] Fanlu Meng,[ab] Xinbo Zhang,* [a] Junmin Yan*[b] and Qing Jiang[b]

Received 15th March 2017,
Accepted 11th April 2017

DOI: 10.1039/c7qm00119c

rsc.li/frontiers-materials

The urgent need for clean and renewable energy and environmental awareness have promoted extensive research into creating a future sustainable energy supply system. Water electrolysis, considered the most promising technology for hydrogen production, has attracted much attention. A series of metal–nitrogen–carbon based heterogeneous electrocatalysts have been developed for HER and OER. Recent advances in this field are summarized here, including their structures, synthetic methods and especially highlighting the applications of several major kinds of catalysts in water splitting. Finally, the existing key challenges and research directions for enhancing performance are pointed out.

1. Introduction

With the continuous increase in energy demand and related environmental issues, creating a global-scale sustainable energy system for the future is one of the most crucial challenges.[1–4] Hydrogen has been regarded as the future energy carrier due to its highest energy density per mass and pollution-free by-product.[5,6] Moreover, among the current main pathways for industrial hydrogen production,[7] water electrolysis, preferably coupled with renewable energy resources, is considered the most promising technology for hydrogen production, which is consistent with future sustainable energy supply, as its feedstock, water, is an abundant and renewable hydrogen source.[8–10] Electrochemical water splitting can be divided into two half-reactions: the hydrogen evolution reaction (HER) and the oxygen evolution reaction (OER) on the cathode and anode, respectively. Although this technology can meet our various harsh requirements, the influence of many factors means it suffers from high cost and low energetic efficiency.[11–13] Thus, seeking efficient catalysts to drastically accelerate the reaction and improve the efficiency in a moderate manner are highly desirable in addition to continuous technological improvement.

Currently, the state-of-the-art HER and OER catalysts are Pt-group metals and Ir- or Ru-based compounds, respectively,[14,15] but their long-term availability is questionable because of their scarcity and subsequent prohibitive price, as well as their limited stability.[16,17] Therefore, substantial efforts have been devoted to developing non-noble metal electrocatalysts with

[a] State Key Laboratory of Rare Earth Resource Utilization, Changchun Institute of Applied Chemistry, Chinese Academy of Sciences, Changchun 130022, China. E-mail: xbzhang@ciac.ac.cn; Fax: +86-431-85262235; Tel: +86-4385262235
[b] Key Laboratory of Automobile Materials, Ministry of Education and College of Materials Science and Engineering, Jilin University, Changchun 130022, China

Kaihua Liu

Kaihua Liu received his BS degree in college of chemistry and materials science from Ludong University in 2013. He is currently pursuing his PhD in Materials Science at Jilin University of China and Inorganic Chemistry at Changchun Institute of Applied Chemistry, Chinese Academy of Sciences, under the supervision of Prof. Junmin Yan and Prof. Xin-Bo Zhang. His research focuses on the development of nanomaterials for energy conversion applications.

Haixia Zhong

Haixia Zhong has received her PhD under the supervision of Prof. Xin-Bo Zhang at Changchun Institute of Applied Chemistry, Chinese Academy of Sciences. Her research interests focus on developing cost effective counterparts as alternatives to precious catalysts for some key electrocatalysis processes like oxygen reduction, water splitting, and CO_2 reduction reactions.

commensurate performance, and a series of robust catalysts have been well established for either HER[18–22] or OER.[23–26] Among these, metal–nitrogen–carbon (M–N–C) materials, which have emerged as the most promising oxygen reduction catalysts,[27–31] have also gained increasing research interest for water splitting due to their unique properties. Obviously, their high activity mainly depends on the special atomic structures of M–N–C catalysts because of the strong dependency between structure and property. For instance, multi-shelled hollow structures have been extensively synthesized and have achieved high performance in many fields.[32–41] However, relevant reviews about M–N–C structures and their applications in water splitting have still not been published.

In view of the rapid development of this thriving field, a comprehensive review may guide further scientific activities. Herein, we summarize recent progress in M–N–C heterogeneous water-splitting electrocatalysts, including Co–N–C, Ni–N–C, Fe–N–C, alloy–N–C and others. The M–N–C structures and the frequently used synthetic strategies will be introduced first. Then these catalysts for water splitting are described. Last, some scientific challenges that exist in M–N–C heterogeneous catalysts and the outlook for future research are also discussed.

2. Evaluation parameters and M–N–C structure

2.1 Evaluation parameters

To estimate the catalytic activity of target electrocatalysts, some frequently-used parameters should be provided, mainly including overpotential, Tafel slope and exchange current density, turnover frequency, faradaic efficiency, as well as stability. As they have been illustrated comprehensively in many other reviews,[7,42–44] here we explain them briefly.

Fanlu Meng

Fanlu Meng received his BS degree in materials science and engineering from Jilin University in 2012. He is currently pursuing his PhD in Materials Science at Jilin University of China and Inorganic Chemistry at Changchun Institute of Applied Chemistry, Chinese Academy of Sciences, under the supervision of Prof. Junmin Yan and Prof. Xin-Bo Zhang. His current interests include the synthesis and characterization of nanostructures for clean energy conversion reactions.

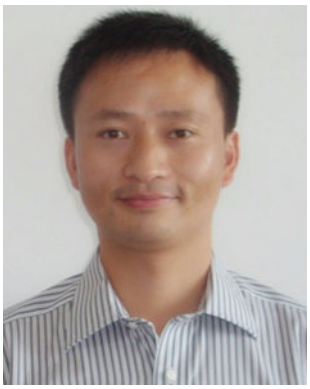

Xinbo Zhang

Dr Xin-Bo Zhang (1978) joined Changchun Institute of Applied Chemistry (CIAC) as a professor of "Hundred Talents Program" of Chinese Academy of Sciences (CAS) in the spring of 2010. He received his PhD degree in inorganic chemistry from CIAC and was granted the CAS Presidential Scholarship Award in 2005. Then, during 2005–2010, he worked as a JSPS and NEDO fellow at National Institute of Advanced Industrial Science and Technology (Kansai Center), Japan. His interests mainly focus on functional inorganic materials for energy storage and conversion with fuel cells and batteries, especially lithium–air batteries.

Junmin Yan

Dr Jun-Min Yan received her PhD degree in inorganic chemistry from Changchun Institute of Applied Chemistry, Chinese Academy of Sciences in 2006. After that, she worked as a JSPS and NEDO fellow at the National Institute of Advanced Industrial Science and Technology, Japan. At the beginning of 2010, she joined the Department of Materials Science and Engineering at Jilin University as a professor of "New Century Excellent Talents in Universities of Ministry of Education of China". Her current research interests focus on the development of new functional materials for (renewable) energy storage and conversion applications.

Qing Jiang

Dr Qing Jiang is the Chueng Kong Scholar Professor of the School of Materials Science and Engineering, Jilin University and Director of the Key Laboratory of Automobile Materials, Ministry of Education, China. He received his BSc and MSc in Materials Science from Jilin University of Technology in 1982 and 1984, respectively, and PhD in Chemistry from University of Stuttgart, Germany in 1990. Later, he has worked as a Postdoctoral Fellow or a visiting professor at Berlin University of Technology, University of California, Irvine, USA, Forschungszentrum Karlsruhe, Karlsruhe, Germany, and Tohuku University, Sendai, Japan.

Firstly, regardless of the media where water splitting takes place, the thermodynamic voltage of water splitting is 1.23 V under standard conditions, but actually a larger potential is needed to push electrochemical water splitting, wherein the excess potential compared to the theoretical potential is the overpotential. The potential at which water splitting occurs is the onset potential. However, in most cases, the overpotential needed to reach a current density of 10 mA cm^{-2} is often used to compare the catalytic activity of catalysts, and this is the metric relevant to solar fuel synthesis. Next, the Tafel slope and exchange current density which are two important kinetic parameters can be obtained from the Tafel equation. The possible rate-determining reaction mechanism of the catalyst can be deduced from the Tafel slope, and the exchange current density is correlated to the intrinsic catalytic activity of the electrode material under equilibrium conditions. In brief, an efficient electrocatalyst usually possesses a low overpotential, small Tafel slope and high exchange current density. In addition, the catalytic activity of an individual active site can be deduced from the turnover frequency, which is defined as the number of reactants that a catalyst can convert to a desired product per catalytic site per unit of time. However, it is always difficult to garner the precise turnover frequency, as the heterogeneously electrocatalytic reaction always occurs at the surface of the electrode. As for the faradaic efficiency, it is the ratio between the experimental and theoretical hydrogen production. Thus, the theoretical production can be calculated from galvanostatic or potentiostatic electrolysis and the practical production can be obtained by gas chromatography. Most of the faradaic loss originates mainly from heat loss or the formation of other products. Stability is another critical parameter for practical applications, and it can be characterized by two simple electrochemical techniques: cyclic voltammetry and galvanostatic/potentiostatic electrolysis. Generally, stable catalysts should offer a current density larger than 10 mA cm^{-2} for more than 10 h or over 5000 cyclic voltammetry cycles.

2.2 M–N–C structure

Initial research into M–N–C complexes can be traced back to 1964 when it was found that Co–phthalocyanine exhibited oxygen reduction activity.[45] Since then, numerous efficient M–N–C catalysts, based on different research directions, such as synthetic methods and mechanistic study, have been widely discussed.[46–49] However, the active site structure and catalytic mechanism of these M–N–C catalysts are still hard to illustrate clearly.[50] Possible reasons may be that the non-crystallographic ordering of the metal atoms is difficult to confirm, as well as the disturbance of the simultaneous presence of other metal-based phases. However, poisoning of M–N–C catalysts by cyanide indicated the metal-based nature of the activity.[51] Generally, the catalytic activity sites of M–N–C catalysts are the M–N_x and N defects. Based on previous studies, some molecular structures have been proposed. For instance, in the case of Fe–N–C catalysts, the FeN_4 species were detected by Time of Flight Secondary Ion Mass Spectrometry.[52] And then, several Fe–N_x species have also been proposed based on Extended X-ray

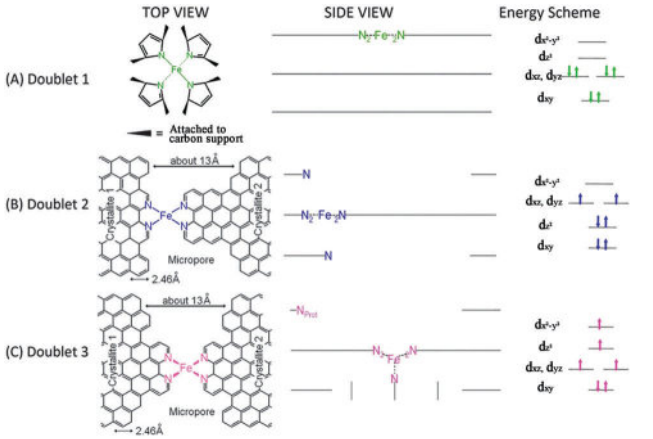

Fig. 1 Side views and top views of the proposed structures of: (A) an FeN_4/C catalytic site in heat-treated, macrocycle-based catalysts assigned to the Mössbauer doublet D1, (B) the FeN_{2+2}-like micropore-hosted site found in a catalyst prepared with iron acetate and heat-treated in ammonia assigned to doublet D2, and (C) a N–FeN_{2+2}-like composite site, where N–FeN_{2+2} is assigned to doublet D3. In all side views, graphene planes are drawn as lines.

Absorption Fine Structure (EXAFS) and Mössbauer spectroscopies, as shown in Fig. 1.[53] Briefly, three doublets, the ferrous ions in a low (D1), intermediate (D2) or high (D3) spin state, were assigned to molecular FeN_4-like sites, and two other doublets (D4 and D5) were assigned to surface oxidized nanoparticles of iron nitride (Fe_xN, $x \leq 2.1$). In addition, another Fe-species, attributed to incomplete FeN_4-like sites, appears only in the catalysts with Fe-contents $\geq$0.27 wt%, which can quickly dissolve in contact with an acid. Thus, most of D2, D4 and D5 can be also removed after acid washing of the original Fe–N–C catalysts, but the D1 and D3 are much more acid-resistant.

Recently, Zitolo *et al.* investigated the structure of active sites in Fe–N–C catalysts which were pyrolysed in Ar or NH_3.[54] The EXAFS result indicated that the best-fit analysis was 5-fold and 6-fold coordination (Fig. 2). While the results of X-ray absorption near-edge spectroscopy (XANES) spectra, reported in Fig. 3, displayed an excellent agreement between experimental and theoretical spectra. Thus, the structure of two candidate active sites having a porphyrinic planar architecture with an FeN_4C_{12} core and with dioxygen adsorbed in the side-on or end-on configuration was provided, which was in strong contrast with the previously assumed FeN_xC_y moieties based on N atoms included in six membered rings. Even though other FeN_xC_y moieties may be present in other systems, important constraints limiting the remaining degrees of freedom were also proposed. First, the coordination number of Fe with a light atom (C, N or O) is 5–6 in the first coordination sphere, while in the second coordination sphere it is larger than 10, thus demanding that the C–N–C bond angles should be smaller than 120°. Subsequently, the absence of the pre-edge peak needs axial ligands breaking the D_{4h} symmetry. This is a major step towards an understanding of the Fe–N–C structure.

Very recently, Zhang *et al.* synthesized a single-atom dispersed Co–N–C catalyst.[55] Since Co was dispersed exclusively as single

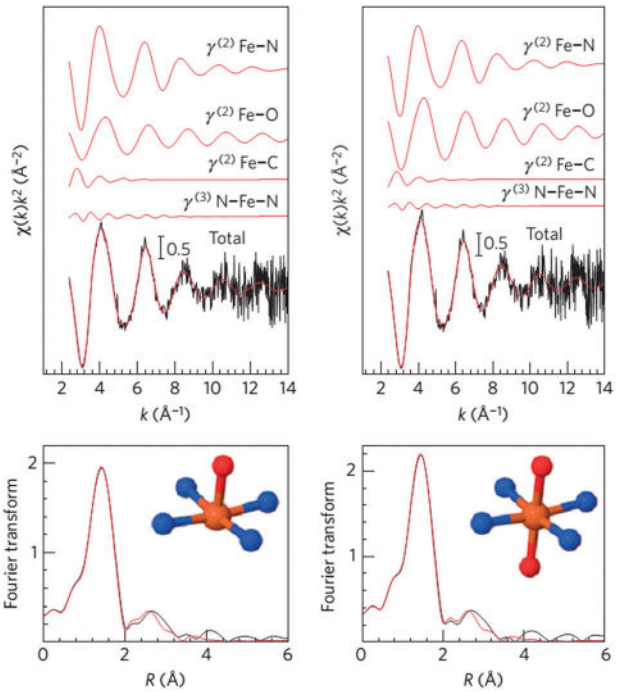

Fig. 2 Fe K-edge EXAFS analysis of $Fe_{0.5}$ with an FeN_4 moiety having one (left) or two (right) oxygen atoms in the axial direction.

atoms, the structure of this Co–N–C was identified to be CoN_4C_8-1-2O_2, where the Co center atom was coordinated with four pyridinic N atoms in the graphitic layer, while two oxygen molecules were weakly adsorbed onto Co atoms perpendicular to the Co–N_4 plane. This was shown by means of sub-Ångström-resolution high-angle annular dark field aberration-corrected scanning transmission electron microscopy (HAADF-STEM) in combination with XANES and EXAFS analysis, as shown in Fig. 4. Based on these considerations, the M–N–C structure might be related to many factors, such as the synthesis process, so the exact nature of the M–N–C structures is still being debated.

3. Synthetic strategies

The most common method to fabricate M–N–C nanostructures is heat-treatment of the related precursors. According to the different precursors, the methods can be divided into two categories. One is the pyrolysis of metal macrocycles complexes, and another is the preparation by direct pyrolysis of a mixture of metal salts, N- and C-containing precursors.

3.1 Pyrolysis of metal macrocycles complexes

Typically, ideal M–N–C catalysts always possess a large number of M–N_4 sites in the carbonaceous matrix and a minimum number of metal nanoparticles. In addition, the carbon supports, which can affect the mass transportation, active site distributions and overall conductivity, also play a critical role in the catalytic reaction.[56] Originally, heat-treatment of the transition metal macrocycles has always been carried out to synthesize M–N–C catalysts, such as Fe and Co porphyrins or phthalocyanines.

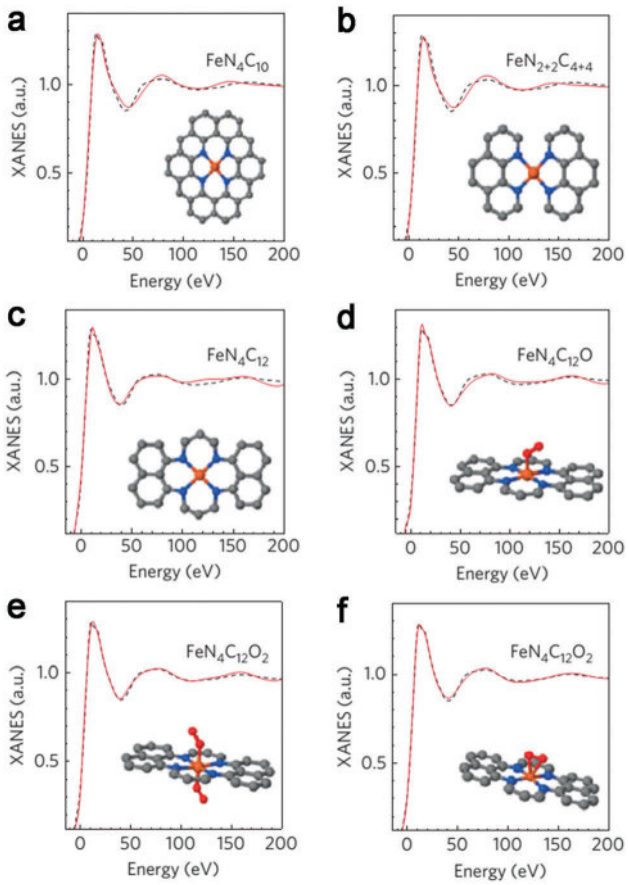

Fig. 3 Comparison between the K-edge XANES experimental spectrum of $Fe_{0.5}$ (black dashed lines) and the theoretical spectrum calculated with the depicted structures (solid red lines). (a) FeN_4C_{10} moiety. (b) $FeN_{2+2}C_{4+4}$ moiety. (c) FeN_4C_{12} moiety. (d) FeN_4C_{12} moiety with one O_2 molecule adsorbed in end-on mode. (e) FeN_4C_{12} moiety with two O_2 molecules adsorbed in end-on mode. (f) FeN_4C_{12} moiety with one O_2 molecule adsorbed in side-on mode.

For instance, the feasibility of heat-treated carbon-supported Co tetramethoxyphenylporphyrin (CoTMPP), a typical macrocycle, was investigated,[57] and then Zhang *et al.* adopted ultrasonic spray pyrolysis to synthesize spherical and porous carbon-supported CoTMPP catalysts,[58] which exhibited a specific surface area which was twice as large as that of the conventional sample.

3.2 Pyrolysis of mixtures of M-, N- and C-precursors

Another synthesis method to prepare M–N–C catalysts is direct pyrolysis of a mixture of related metal salts, N- and C-containing precursors. And based on the different N sources, they can be divided into inorganic N sources and organic N sources.

3.2.1 Inorganic N sources. The most commonly used inorganic N source is NH_3. At a high pyrolysis temperature, NH_3 can preferentially gasify the disordered carbon support. Dodelet *et al.* synthesized a Fe–N–C catalyst by wet impregnation of Fe(II) acetate on carbon black, followed by heat treatment in NH_3.[59] Because the micropores produced during pyrolysis have significance effects on the catalytic reaction, this group filled the pores of the microporous carbon support with pore filler

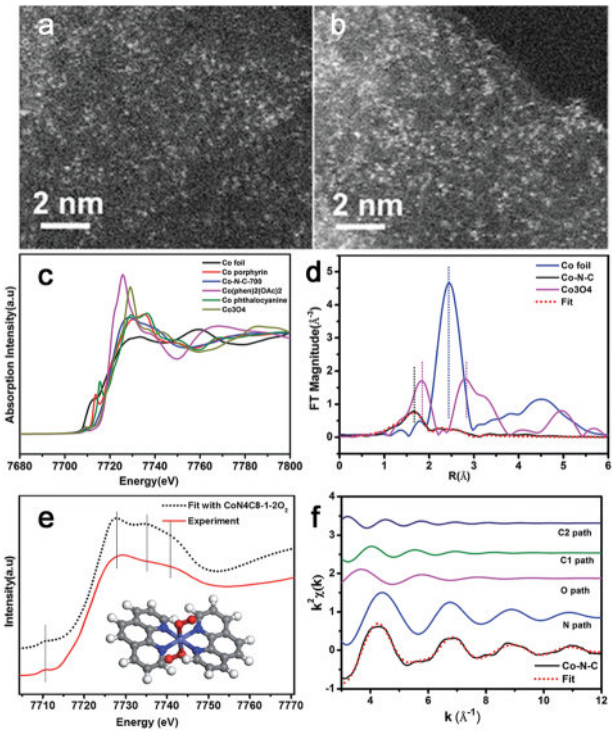

Fig. 4 HAADF-STEM (a and b) images of Co–N–C catalyst. The white dots in (a and b) are Co single atoms. (c) The normalized XANES spectra at the Co K-edge of different samples. (d) The k^2-weighted Fourier transform spectra of the experimental and fitted Co–N–C catalyst as well as the Co foil and Co_3O_4 reference samples. (e) Comparison between the K-edge XANES experimental spectrum of Co–N–C (solid red line) and the theoretical spectrum (black dotted line) calculated with the inset structure. (f) The contributions of different paths including Co–N (blue line), Co–O (pink line) and Co–C (green and navy blue lines) in k-space for the Co–N–C sample.

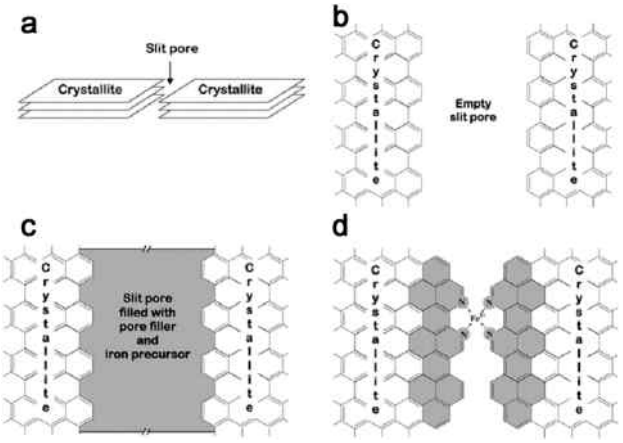

Fig. 5 Schematic representation of catalytic site formation in the micropores of the carbon support. (a) Simplified 3D view of a slit pore between two adjacent graphitic crystallites in the carbon support. (b) Plan view of an empty slit pore between two crystallites. (c) Plan view of a slit pore filled with pore filler and iron precursor after planetary ball-milling. (d) Plan view of the presumed catalytic site (incomplete) and graphitic sheet growth (shaded aromatic cycles) between two crystallites after pyrolysis.

and Fe precursor by planetary ball-milling, and then heat treatment in NH_3 to obtain the Fe–N–C catalyst (Fig. 5).[60] In addition, sodium azide can also be used as an inorganic N source. Bao *et al.* encapsulated Fe nanoparticles into pod-like carbon nanotubes (CNTs) *via* a one-step synthesis at only 350 °C in N_2 with ferrocene and sodium azide as the precursors.[61] And they also used ammonium hexacyanoferrate(II) hydrate as a precursor to improve the N content in the catalyst.

3.2.2 Organic N sources. Compared with inorganic N sources, many N-containing organic molecules can be used as N sources, such as imidazole, pyrrole, melamine, polyaniline and polydopamine. For instance, an Fe–N–C catalyst can be prepared by pyrolysis of carbon black supported Fe–imidazole complexes.[62] Lee *et al.* used the pyrolysis of commercially available melamine foam, Fe salt and carbon black as precursors to create Fe–N–C catalysts with unique architectures and large pore volume.[63] Meanwhile, Fe_3C is also present in the catalysts under these synthesis conditions. Lu *et al.* also synthesized Fe@Fe_3C–N–C spheres with micropores and mesopores by using polydopamine as the C and N sources.[64] In addition, polyaniline, aromatic rings connected *via* N-containing groups, in a similar structure to graphite, have also been selected as the C and N templates. Furthermore, the incorporation of N uniformly distributed into a partially graphitized carbon matrix is ensured because of the use of a polymer as the N precursor. So Wu *et al.* prepared the M–N–C catalyst *via* heat treatment of Fe- and Co-based catalysts in the presence of polyaniline.[31,65] What is more, their result also demonstrated that simultaneous heat treating was beneficial for improving the activity.[31]

In general, the intrinsic advantages of mesoporous materials, such as mesopores and high specific surface areas, are beneficial for high-flux mass transportation and efficient utilization of active catalytic sites. So porous M–N–C materials were often prepared and generally used in the template-assisted synthesis route. For example, ordered hierarchically porous Fe–N-embedded graphitic architectures were synthesized by pyrolysis of 2,2-bipyridine and Fe salt in confined mesochannels of SBA-15, and then etching of the templates (Fig. 6a).[66] This preparation method can produce an *in situ*-formed carbon matrix with a uniform distribution of catalytically active sites on the complete surface. However, the template removed is trivial, time-consuming and uses dangerous acids or alkalis. In this context, our group fabricated Fe–N–mesoporous carbon microspheres *via* carbonization of Fe-modified polypyrrole mesoporous microspheres, wherein the Fe_3O_4 mesoporous microspheres were simultaneously employed as the mesoporous structure directing agent, the source of Fe^{3+} ions which is the oxidation agent for the polymerization of pyrrole, and the Fe precursor (Fig. 6b).[67] Finally, a porous structure with a homogeneous Fe and N species distribution was obtained by this facile *in situ* replication and polymerization strategy (Fig. 6c and d).

In addition, considering their elemental composition and structural advantages, metal–organic frameworks (MOFs), which inherently possess metal, N– and C– in the backbone, an ordered structure, higher surface area and tunable porosity, are no doubt the ideal precursors to fabricate efficient M–N–C catalysts.[50,56,68]

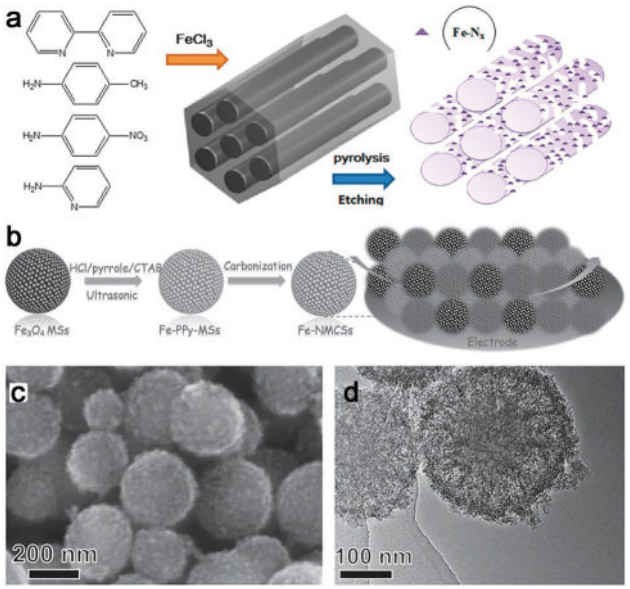

Fig. 6 (a) Synthesis of ordered hierarchically micro- and mesoporous Fe–N–GC materials. (b) Schematic representation of the preparation process of an Fe–NMCSs catalyst. (c and d) SEM and TEM images of Fe–NMCSs.

Importantly, M–N–C catalysts can be derived from direct calcination of the relevant MOF precursors, especially for Fe–N–C and Co–N–C. Thus, calcining MOFs to obtain M–N–C composites has been widely used.[69–71]

3.3 Other synthetic methods

Though the above pyrolysis methods can directly obtain M–N–C catalysts, there are also many questions, such as the reproducibility and precise composition control. Therefore, a search for facile and high-temperature free synthesis methods should be considered. As shown in Fig. 7, the Qiao group prepared N-doped graphene film-confined Ni nanoparticles by a heterogeneous reaction process.[72] First, the graphene film was impregnated with $Ni(NO_3)_2$ and $NH_3{\cdot}H_2O$, and then heated to obtain the precursor film. Subsequently, the precursor film was doped and reduced *via* the solvothermal reaction with $N_2H_4{\cdot}H_2O$. Searching for diversified synthetic strategies to construct various special structures still plays a crucial role in their practical application.

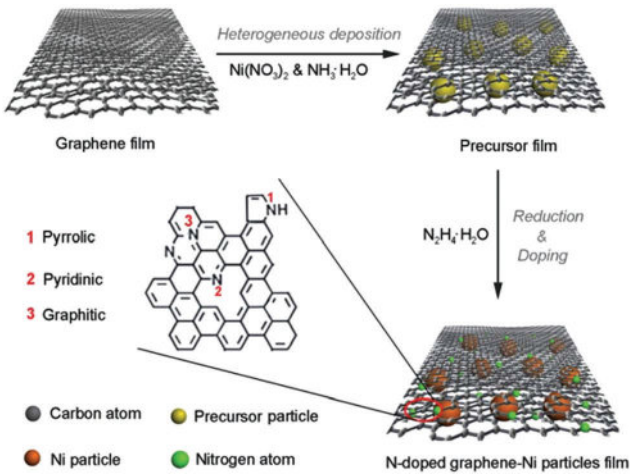

Fig. 7 Fabrication of a 3D Ni–NG electrode.

4. Applications of M–N–C catalysts in water splitting

Compared with the extensive study of M–N–C catalysts in oxygen reduction, recently the application of M–N–C materials in water splitting has attracted broad interest, and some progress has been achieved. Considering the synthetic process and elemental composition, the presence of some metals, such as Co and Fe, can catalyze the formation of N–C nanostructures, such as CNTs. Thus, metal embedding, N doping and their synergistic effect, which can regulate the H-bonding energy and electrical conductivity, all contribute to improving the electrocatalytic performance. Furthermore, in most cases, the metal is protected by the carbon layers, which is beneficial for avoiding corrosion and oxidization and preventing agglomeration, as well as for the stability of the catalysts. Accordingly, M–N–C composites may be promising water splitting electrocatalysts.

4.1 Co–N–C materials

Co–N–C materials have been widely researched for HER[73–83] and OER,[84–90] as well as for full water splitting catalysts.[91–97] Thanks to their structural advantages, Co–N–C complexes can be used as efficient HER catalysts at various pH values. For example, Co nanoparticles encapsulated in a Co and N co-doped carbon catalyst (Co@Co–N–C) displayed an onset potential of 78 mV with a Tafel slope of 59 mV dec^{-1} in 0.1 M KOH solution.[76] While N–C wrapped Co nanoparticles supported on N-doped graphene (Co@NC/NG) showed an onset potential of 49 mV with a Tafel slope of 79.3 mV dec^{-1} in 0.5 M H_2SO_4, and theoretical studies implied that the catalytically active sites likely arose from carbon atoms promoted by the entrapped Co nanoparticles.[77] Other work also suggested that the transition metals and N played a critical role in the enhanced activity based on results from electrochemical and DFT calculations.[81] In addition, most of these types of catalyst can be used as HER catalysts in both alkaline and acidic media,[74] and even neutral electrolytes.[75,79,82,83]

Zou *et al.* first reported CNT-based Co–N–C electrocatalysts (Co–NRCNTs) for HER.[75] As shown in Fig. 8a–d, the Co–NRCNTs exhibited high HER activity and stability over the whole pH range. In addition, the origin of the superior HER activity of Co–NRCNTs was also investigated. An increase in the pyrolysis temperature caused the HER activity to decrease, which was consistent with the defect density and N content in the catalysts except for the unchanged Co content (Fig. 8e–h). The influence of metal nanoparticles was revealed based on the catalytic activities (Fe–NRCNTs < Ni–NRCNTs < Co–NRCNTs) which was tested under the same conditions. These results indicated that the embedded Co particles, N dopants, and synergistic effects between them all contributed to the excellent HER activity.

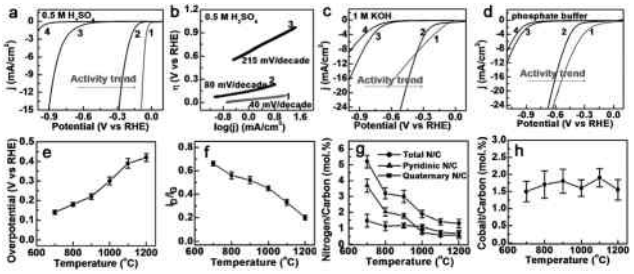

Fig. 8 (a) Linear sweep voltammetry (LSV) curves in 0.5 M H_2SO_4 (pH 0), (b) the corresponding Tafel plots in H_2SO_4 solution, and LSV curves in (c) 1 M KOH (pH 14) and (d) phosphate buffer (pH 7) solutions. Sample labels are: (1) 1 wt% Pt/C; (2) Co–NRCNTs; (3) MWCNTs; and (4) no catalyst. (e) Catalytic activity in 0.5 M H_2SO_4 (pH 0) as a function of the pyrolysis temperatures employed to synthesize the carbon nanomaterials. (f) The I_D/I_G value (obtained from FT-Raman spectra), (g) the ratios of total N/C, pyridinic N/C and quaternary N/C (obtained from XPS), and (h) the ratio of Co/C (obtained from thermogravimetric analysis) as a function of pyrolysis temperatures.

Nevertheless, a mechanistic investigation to reveal the real reasons, especially on the atomic level, is still needed.

Increasing the surface area to provide more active sites, Liang *et al.* prepared a porous Co–N–C catalyst with a high specific surface area (1074 $m^2\ g^{-1}$) (Fig. 9a).[83] Undoubtedly, this catalyst displayed an outstanding HER performance at all pH values, such as 10 mA cm^{-2} achieved at an overpotential of 133 mV in acid, and unprecedented TOFs (TOFs per Co atom of 0.39 and 6.5 s^{-1} at an overpotential of 100 and 200 mV, respectively) (Fig. 9b and c). Moreover, thiocyanate ions (SCN^-), which can poison the metal-centred catalytic sites in acid, were adopted to demonstrate that the active sites are CoN_x centres (Fig. 9d and e). However, as they noted, there is still large room for further improvement in the HER performance of M–N–C catalysts, such as optimizing the M–N binding or increasing the density of MN_x sites. Recently, single-atom catalysis has attracted increasing attention because of the lowest size limit to obtain full atom utility, and decreasing the nanoparticle size can also expose more active sites. Thus Co atoms, coordinated to N atoms on graphene, were prepared and exhibited high HER performance in both acidic and basic solutions.[98]

One novel two-dimensional carbon allotrope, graphdiyne (GD), has attracted much attention due to its special composition of a one-atom thick layer of sp- and sp^2-hybridized carbon atoms.[99–101] Thanks to its special structure, GD exhibits intriguing properties, such as a unique electronic structure, electrical conductivity, and high chemical stability. Thus, it has been applied in many fields.[102–105] Recently, GD nanosheets supporting Co nanoparticles wrapped in N-doped C (CoNC/GD) were fabricated as HER catalysts.[106] Impressively, this catalyst displayed superior HER performance and unprecedented durability, which could be indicated by the negligible current change over 36 000, 38 000, and 9000 cycles under basic, acidic, and neutral conditions,

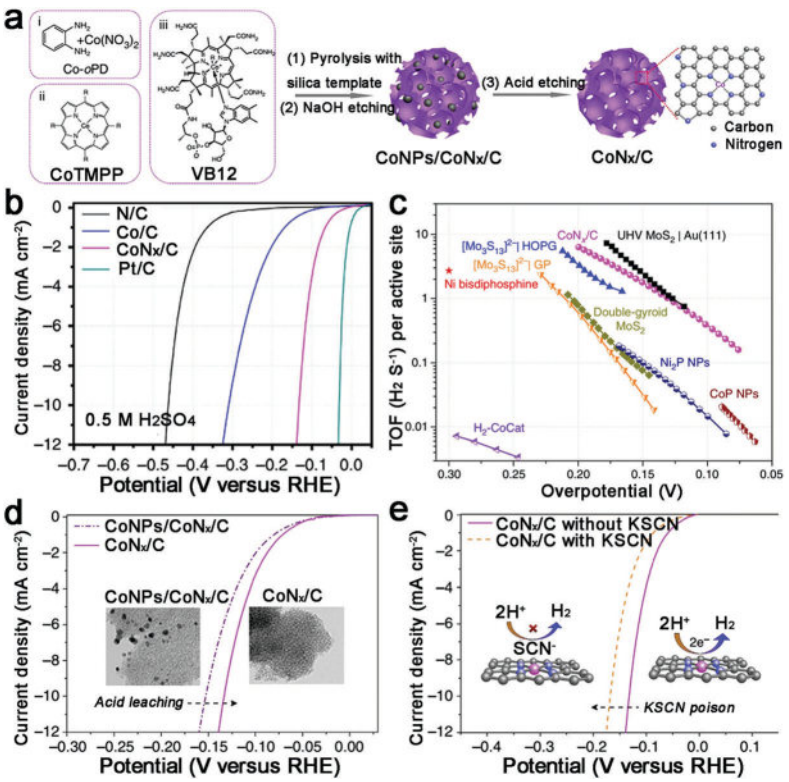

Fig. 9 (a) Schematic illustration of the synthesis of CoN_x/C electrocatalysts. (b) HER polarization plots of CoN_x/C, N/C, Co/N and Pt/C catalysts in 0.5 M H_2SO_4. (c) Comparison of the TOF of CoN_x/C with other catalysts. (d) Comparison of the HER activity of $CoNPs/CoN_x/C$ and CoN_x/C catalysts, showing the influence of acid leaching. Insets are TEM images demonstrating that all Co particles were removed by acid leaching. (e) HER polarization plots of CoN_x/C with and without 10 mM KSCN in 0.5 M H_2SO_4.

respectively. Finally, the outstanding HER behaviors of CoNC/GD could be explained as follows: (1) the unique electronic structure and high conductivity of the GD nanosheets make them highly conductive supporting matrices. (2) The high porosity of the GD structure ensures efficient mass transport. (3) The Co atoms interacting with the alkyne rings facilitate rapid electron transfer from the Co atoms to the GD sheets. (4) The intimate contacts of the Co atoms with both the GD nanosheets and the N-doped C coatings provide more catalytically active sites and enhance the stability.

As for the typical interface reaction, activating the outermost carbon layer and engineering the surface active sites are efficient means to improve activity. Thus, Co nanoparticles encapsulated by N and B codoped ultrathin graphitic carbon cages were constructed.[73] Surprisingly, the Co@BCN showed extraordinary HER activity with an onset potential of about 0 V, an overpotential of 96 mV to achieve 10 mA cm^{-2}, and a Tafel slope of 63.7 mV dec^{-1} in 0.5 M H_2SO_4. In addition, the poisoning test with SCN^- revealed that the B, N codoped carbon shell contributed significantly more than a trace of uncoated Co species to the enhanced HER activity, which should be the major active sites in this catalyst. Finally, based on the DFT calculations, the encapsulation of Co nanoparticles by an outer carbon shell modifying the electronic Fermi level, and the codoping of N and B heteroatoms generating additional active sites, produced a synergistic effect to optimize the ΔG_{H^*}, and hence improved the HER activity.

To avoid burying the active sites and low electron contact surface area caused by the insulated polymer binder, and even alleviating the gas accumulations for stabilizing the electrode during electrolysis process, 3D integrated HER electrodes are always actively pursued. N–C coated Co nanorod arrays supported on titanium mesh (Co@NC/Ti) were prepared and showed high activity over a wide pH range.[80] To further optimize the electrode structure, our group fabricated a self-supported and 3D porous structure of Co–N–C catalysts (only 0.22 at% Co), which displayed excellent HER performance, especially in acid (212 mV at 100 mA cm^{-2}) and long-term stability (Fig. 10a–c).[82] Importantly, the structure of the active sites was investigated by XANES and EXAFS spectroscopy (Fig. 10d–f). The Co K-edge XANES spectra suggested the possible existence of Co–C/N species, and Co–C and Co–N bonds coexisting in the active Co complex were demonstrated by the XAFS results, which also indicated that the total coordination number was five. Then, DFT calculations were performed to investigate the catalytic mechanisms of this complex. As a result, Co–3C1N showed a high density of states crossing the Fermi level, which contributed to electron mobility, and a moderate free energy for H adsorption compared with Co–4C and Co–4N (Fig. 10g). Based on these results, the excellent HER activity was mainly attributed to the synergistic effect of the C and N hybrid. Moreover, considering the preparation of robust catalysts with low metal content, an interconnected Co–NCNT film on CC (Co–NCNT/CC) was designed and showed excellent HER performance and durability over the whole pH range with 10 mA cm^{-2} achieved at overpotentials of 78, 170, and 180 mV in acidic, neutral and alkaline electrolytes, respectively.[78]

The Co–N–C complex was also studied with respect to OER, which severely constrained the overall energy efficiency. Co and N codoped graphene with inserted carbon nanospheres was synthesized and showed an overpotential of 426 mV at 10 mA cm^{-2}.[85] And then to provide a high specific area and a shorter diffusion distance, a Co–N–C catalyst with hollow tetragonal microstructure was constructed, which exhibited high OER activity and stability with an overpotential of 390 mV at 10 mA cm^{-2}, as well as negligible potential change under 10 h of continuous galvanostatic electrolysis.[88] Another strategy to improve the catalytic activity is to decrease the charge transfer resistance.[89] In addition, a Co–N–CNT catalyst was also prepared and displayed an overpotential of 300 mV to achieve a current density of 10 mA cm^{-2} in neutral, and 50 mA cm^{-2} in alkaline media, respectively.[84]

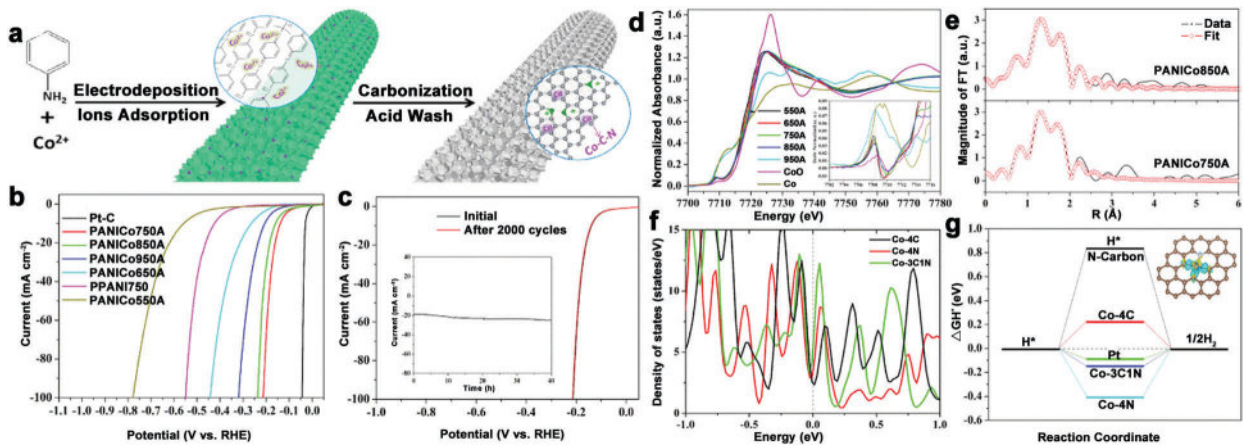

Fig. 10 (a) Schematic illustration of the synthetic process. (b) Polarization curves of PPANI750, PANICo550-950A, and Pt/C in 0.5 M H_2SO_4. (c) Cycle stability measurement. Inset in (c) is the time-dependent current density curve under a constant potential of −0.17 V for 40 h. (d) Normalized XANES spectra near the Co K-edge of Co–C–N samples prepared at different temperatures after acid washing, and Co K-pre-edges enlarged in the inset. (e) FT-EXAFS spectra at the Co K-edge of PANICo750A and PANICo850A and their fitted curves. (f) Density of states of Co–3C1N, Co–4C, and Co–4N complexes. (g) Calculated free-energy diagram of HER at the equilibrium potential for the four catalysts, and the inset is the model structure of the Co–3C1N catalyst.

The transition-metal oxides always show good OER catalytic activity. Thus, Co@Co_3O_4 encapsulated in *in situ* formed N–CNT-grafted carbon polyhedra was fabricated.[86] Thanks to the highly graphitic nature of CNT-grafted polyhedra, the introduction of N and Co, and the synergy between conductive metallic Co cores and semiconductive Co_3O_4 shells which produced a Schottky barrier between them, which is beneficial for charge separation, this catalyst exhibited high OER performance with 10 mA cm^{-2} at 1.64 V, and excellent durability with no significant loss in activity after 45 h. What is more, this catalyst can be directly grown on Ni foam to construct a 3D integrated OER electrode, which displays a better OER stability with a potential of 1.62 V at 10 mA cm^{-2}.

The above study only focuses on one of the two half reactions without considering full water splitting. The N-doped graphene/Co-embedded porous carbon polyhedron (Co–NC/NRGO) was prepared, and showed superior performance for HER with an onset overpotential of 58 mV and a current density of 10 mA cm^{-2} at 229 mV in acid media, as well as good catalytic performance for OER in alkaline media with a potential of 1.66 V for 10 mA cm^{-2}.[91] However, the activity of HER and OER in the same electrolyte was not discussed. Developing electrocatalysts for both HER and OER in the same electrolyte to achieve efficient overall water splitting is no doubt highly imperative. The Bao group took a further step towards the application of Co–N–C catalysts in overall water splitting. They reported that Co nanoparticles encapsulated in N-doped C (Co@N–C) exhibited high HER activity and durability over a wide pH range, as well as good OER performance in alkaline medium.[94] Furthermore, an electrolyzer prototype using Co@N–C as a bifunctional catalyst was built, and displayed considerable activity for water electrolysis at 80 °C (Fig. 11). After that, Co embedded in porous N-rich C (PNC/Co)[93] and a Co–N–C complex interlinked by CNTs (Co–NC/CNT)[95] were prepared and afforded a water-splitting current of 10 mA cm^{-2} at cell voltages of 1.64 V and 1.625 V, respectively.

Co/Co oxide–N–C composites were also fabricated for overall water splitting.[92,97] Considering the superiority of carbon conductivity, the moderate H-bonding energy of metallic Co, and better OER activity of Co oxide, multi-component Co–Co oxide–N-doped carbon hybrids (CoO_x@CN) were synthesized.[97] And undoubtedly, this hybrid exhibited outstanding HER activity and stability with a small onset overpotential of 85 mV and 10 mA cm^{-2} achieved at a low overpotential of only 235 mV in 1 M KOH. Impressively, a significantly enhanced OER performance was obtained after a 30 min HER test because of the increase in Co^{2+}. Finally, a water electrolyzer, with CoO_x@CN as the cathode and anode electrocatalyst, was constructed, which achieved ~20 mA cm^{-2} at a voltage of only 1.55 V. Electrocatalytic experiments further indicated that the extraordinary catalytic performance was mainly attributable to the synergistic effect of Co species, the stability of C-encapsulated Co nanoparticles, the introduction of electron-rich N, and the high conductivity of C.

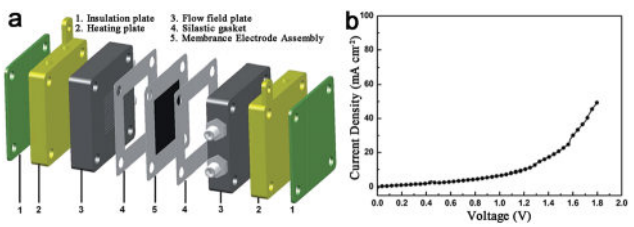

Fig. 11 (a) Schematic configuration of a full water electrolyzer. (b) Polarization curves of water electrolyzer using Co@N–C as both cathode and anode catalysts at 80 °C.

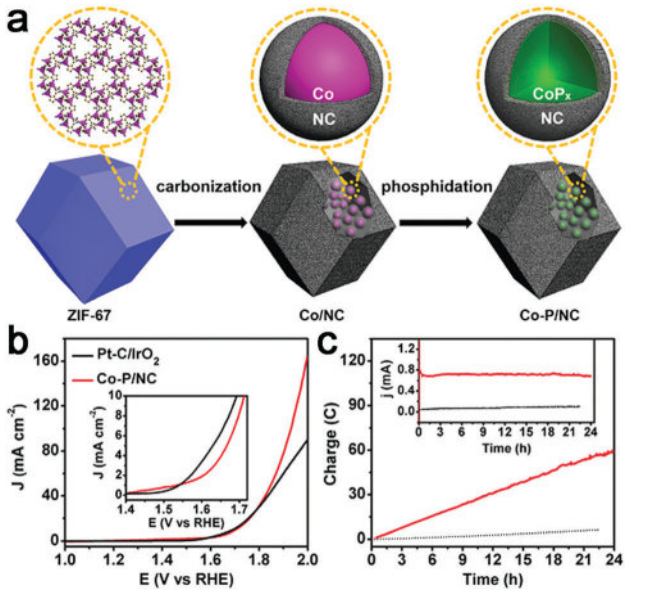

Fig. 12 (a) Illustration of the synthesis of Co–P/NC nanopolyhedrons. (b) Polarization curves of Co–P/NC and Pt/IrO_2 catalyst couples for overall water splitting in 1.0 M KOH. The inset is the expanded region around the onset of catalysis. (c) Long-term controlled potential electrolysis of Co–P/NC in 1.0 M KOH at η = 400 mV. The inset is the corresponding current change over time. Black lines were collected for background electrolysis without Co–P/NC as the electrocatalysts.

Recently, transition metal phosphides have been reported as efficient multifunctional catalysts for water electrolysis. Thus, a Co–P/N–C hybrid was also prepared for overall water splitting.[107,108] Mesoporous Co–P/N–C nanopolyhedrons were synthesized by phosphorization of a Co–N–C complex (Fig. 12a),[107] which exhibited superior catalytic activity to a Co–N–C complex with 10 mA cm^{-2} achieved at an overpotential of 154 mV for HER and 319 mV for OER in 1 M KOH. In addition, this Co–P/N–C based overall water electrolyzer achieved 165 mA cm^{-2} at 2.0 V, superior to that of a Pt/IrO_2 couple, as well as strong stability (Fig. 12b and c). The 3D interconnected mesoporosity, and the CoP_x encapsulated within N-doped C matrices which can be partially oxidized to CoO_x, and are thus beneficial for OER activity, synergistically promote the overall catalytic performance of Co–P/N–C for water electrolysis. A 3D integrated electrode of Co–N–C, followed by phosphorization, was also prepared.[108] However, the activity is still far from satisfactory.

4.2 Ni–N–C materials

With the second highest abundance and lowest price after Fe, metal Ni-based catalysts show the great potential for water

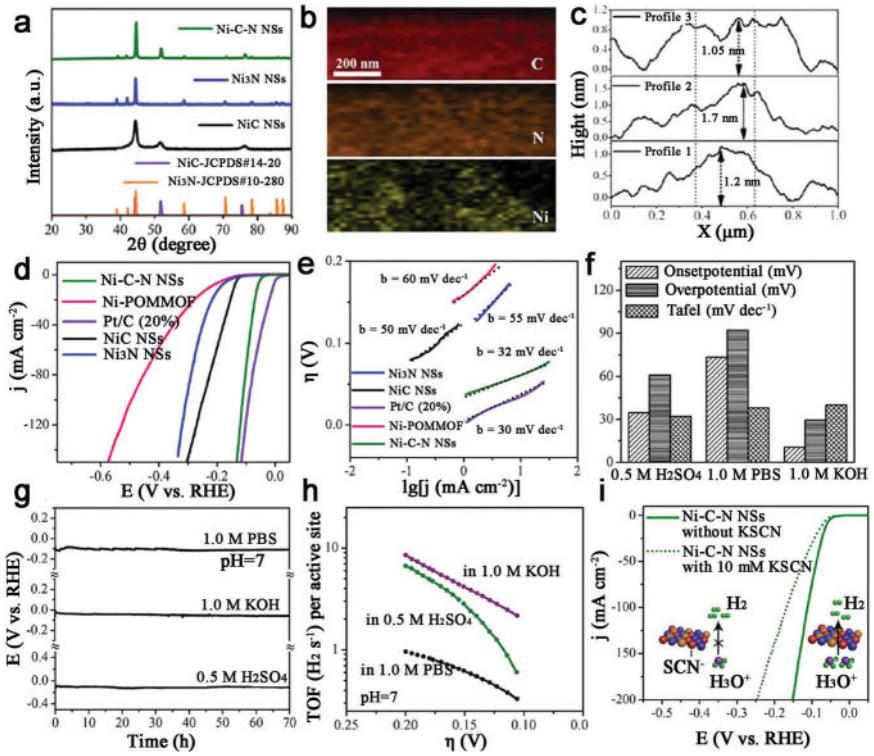

Fig. 13 (a) XRD patterns of hybrid Ni–C–N NSs, NiC NSs, and Ni_3N NSs. (b) Elemental mapping of a selected area of Ni–C–N NS. (c) Height profiles of the exfoliated Ni–C–N NS. (d) LSV HER curves for Ni–C–N NSs, Ni-POMMOF, NiC NSs, Ni_3N NSs, and Pt/C (20%) in 0.5 M H_2SO_4. (e) Tafel plots of different catalysts in 0.5 M H_2SO_4. (f) Summary of onset potential, Tafel slope and overpotential at j = 10 mA cm^{-2} for the HER catalyzed by Ni–C–N NSs in an acid, or neutral, or basic solution. (g) Chronopotentiometric curves of Ni–C–N NSs with a constant current density of 10 mA cm^{-2}. (h) TOF plots of Ni–C–N NSs in different pH conditions (i) LSV HER curves of Ni–C–N NSs with or without 10 mM KSCN in 0.5 M H_2SO_4. Inset: Illustrations of Ni-centers blocked by SCN^- ions.

electrolysis due to their high theoretical activity. Thus, Ni–N–C based catalysts have been studied for HER.[109,110] Sun *et al.* synthesized a new form of hybrid ultrathin Ni–C–N nanosheets (<2 nm) containing NiC and Ni_3N (Fig. 13a–c).[109] And surprisingly, this Ni–C–N hybrid exhibited impressive HER performance over all pH values: for instance, they catalyzed HER in 0.5 M H_2SO_4 at an onset potential of 34.7 mV, with 10 mA cm^{-2} at an overpotential of 60.9 mV and with outstanding long-term stability (~10% current drop after 70 h). A Tafel slope of 32 mV dec^{-1} and an exchange current density of 1.36×10^{-2} mA cm^{-2} were also achieved, as well as a TOF of 6.67 s^{-1} at η = 200 mV (Fig. 13d–h). Moreover, the poisoning experiment with SCN^{-1} confirmed that the Ni-sites were indeed active sites for HER (Fig. 13i). Finally, the author provided a concept that the hybridization of NiC with Ni_3N may contribute to enhancing the catalytic activity, which should be extended to other systems.

Ni–C–N catalysts were prepared and then tuned by an electrochemical method to activate this catalyst to obtain atomically isolated Ni species anchored on graphitized carbon.[111] As a result, the actived catalysts exhibited extraordinary HER performance with 10 mA cm^{-2} at an overpotential of 34 mV, a low Tafel slope of 41 mV dec^{-1} and a large exchange current density of 1.2 mA cm^{-2}, as well as impressive durability, which was attributed to strong chemical and electronic coupling between graphitized carbon and Ni single atoms.

Qiao *et al.* fabricated 3D N-doped graphene film-confined Ni nanoparticle (Ni–NG) catalysts for OER,[72] which displayed an onset potential of 320 mV and an overpotential of 400 mV to approach 16.3 mA cm^{-2}. The catalytic currents of this catalyst were much less affected by scan rates, which indicated the advantage of a 3D architecture for efficient mass and charge transport, but were related to the KOH concentration. In addition, a dual-active-site mechanism was proposed for this catalyst in OER. Firstly, Ni nanoparticles were partly oxidized into NiOOH, and the formed NiOOH/Ni complex species were the active centers, which was beneficial for the oxidation of OH^- into molecular oxygen. Subsequently, the bonding between Ni and N-doped graphene, such as Ni–O–C or Ni–N–C, might produce other active centers due to the high electro-negativity of O or N species which make the adjacent carbon atoms positively charged, which then contribute to adsorbing OH^- *via* electrostatic forces and facilitate water dissociation.

For overall water splitting, a simple Ni–N–C paper electrocatalyst was synthesized using cheap and sustainable cellulose filter paper as the carbon source and material scaffold.[112] This membrane-like, binder-free electrode exhibited 10 mA cm^{-2} achieved at an overpotential of 390 mV, a small Tafel slope of 44 mV dec^{-1}, and considerable stability for OER in 0.1 M KOH. Meanwhile, this catalyst also displayed 10 mA cm^{-2} at an overpotential of 190 mV for HER, which indicated that it was a promising candidate for a symmetric electrolyzer.

4.3 Fe–N–C materials

Compared with the Co–N–C and Ni–N–C based materials, although the Fe–N–C complex shows superior oxygen reduction activity, an investigation shows their water electrolysis performance is relatively poor. A possible reason might be that some Fe–N–C based catalysts exhibited inferior HER activity to Co(Ni)–N–C hybrids under the same synthesis and test conditions.[75,94,113]

The OER activity of Fe–N–C based materials has also been reported. Therefore, the role of Fe for OER in N-doped hollow carbon spheres was discussed.[114] Finally, it was found that Fe contributed to the efficient graphitization of this catalyst structure, which was beneficial for electrocatalytic OER, but may not be necessary for OER. Recently, atomic dispersion of Fe–N_x species on N and S co-decorated hierarchical carbon layers was achieved,[115] and exhibited excellent OER performance with an overpotential of 370 mV at 10 mA cm^{-2} and a Tafel slope of 82 mV dec^{-1} in 0.1 M KOH. The high activity was ascribed to the abundance of atomically dispersed highly active Fe–N_x sites, 3D conductive networks to expedite electron transfer, and unique hierarchical structure to increase active site exposure. Thus, the introduction of S salt also greatly improved the surface area and played a crucial role in synthesizing atomically dispersed Fe–N_x species. In addition, at the high temperature of carbonization, carbide can be easily formed. Thus, Fe–N–C materials based on Fe_3C were reported for OER, but their activities should be improved.[116,117] And bimetal carbide nanoparticles encased in N, P co-doped graphitic carbon (Fe_3C/Mo_2C@NPGC) were also prepared for HER and required an overpotential of 98 mV to achieve 10 mA cm^{-2}.[118]

From another viewpoint, it is well known that optimizing the interaction between the active component and the support could enhance the catalytic performance because of the contributions of the support, such as raising the dispersity of the active sites, facilitating mass-transport and electron-transfer kinetics. M–N–C materials displayed distinct interactions with the intermediates, and the introduction of heteroatoms can tune the electron-donating/withdrawing capability of the carbon basal plane, indicating that M–N–C materials are promising catalyst supports. As a proof-of-concept experiment, our group first used NiO as an active component to evaluate the support effect of M–N–C sheets.[119] Based on experimental observations and DFT calculations the improved activity originated from the low electron-transfer barrier and high electron-coupling capability of the M–N–C sheets. This result demonstrated that the support effect should be considered in designing advanced and cost-effective electrocatalysts, and that M–N–C materials are potential catalyst supports.

Besides the M–N–C materials relying on Fe, Co and Ni, other M–N–C catalysts are also discussed.[120–126] Morozan *et al.* prepared a series of first row transition metal based M–N–C catalysts to investigate the effect of transition metal on the structure and activity for HER.[125] As a result, the type of transition metal played a crucial role in the nature of the obtained carbon so that W, Mo, Cu and Zn led to amorphous carbons with a high specific area while Cr, Mn, Fe, Co and Ni provided more graphitic content in the product with a lower specific area. And among all the M–N–C catalysts presented in this work, the Fe–, Co– and Ni–N–C are the most active in alkaline electrolytes, as shown in Fig. 14a, while Cr and Co based catalysts displayed higher activities in acid (Fig. 14b). And recently, the Qiao group also fabricated a range of molecule-level graphitic carbon nitride coordinated transition metals as a new generation of M–N/C catalysts, which exhibited promising OER performance.[122] To improve the density of catalytically active sites and the effective surface area at the same time, Zhao *et al.* prepared an MoCN material by using an *in situ* CO_2 emission strategy,[123] which exhibited high HER activity with an overpotential of 140 mV at 10 mA cm^{-2} in acid. Similarly, metal carbides (MoC, WC, TaC and NbC) embedded in vertically aligned graphitic carbon nanosheets were also prepared for HER with 10 mA cm^{-2} at 220–250 mV.[124] In addition, inspired by the concept of precious metal recovery from electronic waste, an Au@NC catalyst was designed by bioreduction and then calcination,[121] which exhibited high stability and good HER performance with 10 mA cm^{-2} achieved at an overpotential of 130 mV in acid due to the strong interactions between Au and the carbon substrate, which contributed to charge transfer. Similarly, single Pt atoms on N-doped graphene were also synthesized for HER, and the mass activity exhibited by this catalyst was 37.4 times greater than that of a commercial Pt/C catalyst.[126]

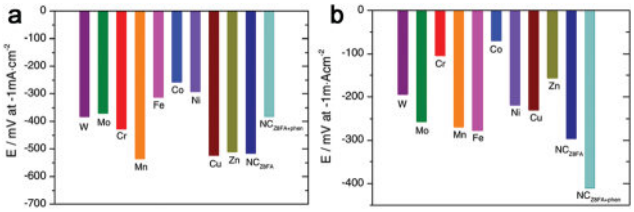

Fig. 14 HER activity at (a) pH 13 and (b) pH 1 for M–N–C and N–C catalysts in the present study.

4.4 Alloy–N–C materials

The alloy phase can not only copy the individual advanced properties, but also usually exhibit amazing catalytic performance because of possible synergetic effects. Thus, alloy–N–C catalysts for water splitting have attracted major interest. And the Bao group has made great contributions to this area. To synthesize ultrathin carbon shells to promote electron transfer from metal cores to the carbon surface, thereby optimizing the electronic structure of the carbon surface, they fabricated a hierarchical architecture in which the uniform CoNi nanoalloy (4–7 nm) was encapsulated in ultrathin graphene shells (only 1–3 layers) for HER in 0.1 M H_2SO_4 (Fig. 15a–d).[127] This catalyst exhibited an overpotential of 140 mV at 10 mA cm^{-2} with a Tafel slope of 105 mV dec^{-1}. The DFT calculations showed a more moderate ΔG_{H^*} for the CoNi@C than for the others, and the nitrogen dopants and metal cores could synergistically optimize the ΔG_{H^*} (Fig. 15e–h). Moreover, the effect of the graphene layer on the HER was also studied by using a model in which a CoNi cluster was encapsulated by one to three graphene layers, as shown in Fig. 15i–k, which showed that the thinner the

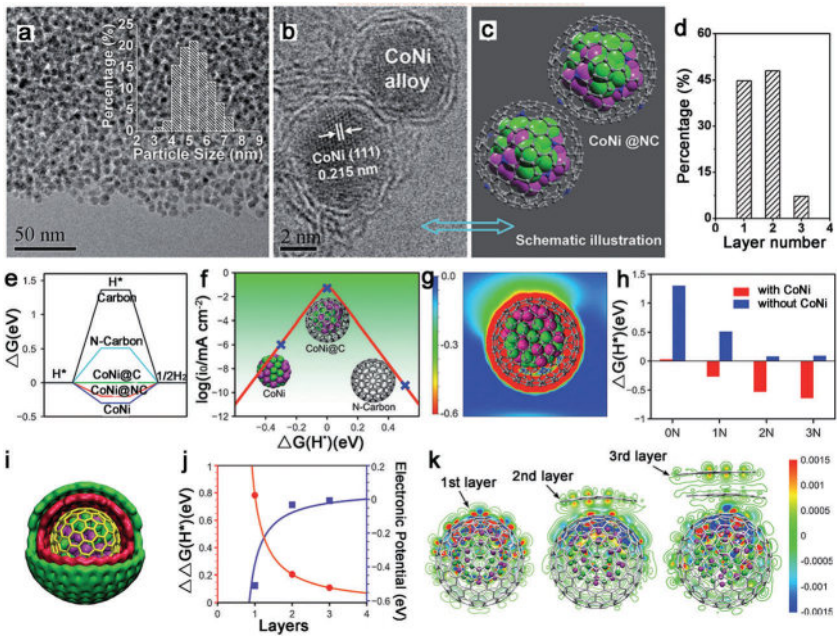

Fig. 15 (a) TEM images of CoNi@NC. Inset: Particle size distribution of the metal nanoparticles. (b) HRTEM images of CoNi@NC. (c) Schematic illustration of the CoNi@NC structure. (d) Statistical analysis of the number of layers in graphene shells encapsulating metal nanoparticles in CoNi@NC. (e) Gibbs free energy profile of HER on various catalysts. (f) Volcano plot of the polarized current *versus* ΔG(H*) for the CoNi cluster, CoNi@C, and N-doped graphene shell. (g) The electronic potential of CoNi@C; the vacuum level was set to zero. (h) The ΔG(H*) on pure and N-doped (one, two, or three N atoms per shell) graphene shells with and without an enclosed CoNi cluster. (i) Schematic illustration of a CoNi alloy encapsulated in three-layer graphene. (j) $\Delta\Delta G$(H*) (red line) and electronic potential (blue line) as a function of the number of graphene layers, where $\Delta\Delta G = \Delta G$(without metal) − ΔG(with metal). (k) Redistribution of the electron densities after the CoNi clusters have been covered by one to three layers of graphene. The differential charge density ($\Delta\rho$) is defined as the difference in the electron density with and without the CoNi cluster. The red and blue regions are regions of increased and decreased electron density, respectively.

graphene shells, the higher the HER performance. Based on these results, decreasing the carbon layer thickness strongly promotes electron penetration from the CoNi nanoalloy to the carbon surface, which contributes to the modulation of the electron density and the electronic potential distribution at the surface accompanied by the N dopants, and then results in superior HER activity.

To further decrease the carbon shell thickness, recently the group also prepared single layer graphene encapsulating metal nanoparticles for OER, including Fe, Co, Ni and their alloys (Fig. 16a–c).[128] Here, the encapsulated FeNi alloy exhibited the best OER activity in alkaline solutions with 10 mA cm^{-2} obtained at an overpotential of only 280 mV, and a high stability after 10 000 CV cycles, which was superior to that of other FeNi–N–C materials (Fig. 16d and e).[69,129] They also fabricated a model and calculated the free energies of various intermediates for OER (Fig. 16f and g). The ΔG(HOO*) and ΔG(HO*) showed a linear relationship (Fig. 16h); thus, the overpotential could be determined from ΔG(O*) − ΔG(HO*). As shown in Fig. 16i, FeNi@C was closest to the volcano peak, indicating the best catalytic performance. And the same trend in calculated overpotential and experimental results suggested that this theoretical model could predict the efficiency of M@C in OER (Fig. 16j).

In addition, Bao *et al.* also embedded FeCo alloy into N–CNTs (FeCo@NCNTs), and the obtained catalyst exhibited stable and high HER activity with an onset potential of 70 mV in acid.[113] The calculated ΔG_{H^*} demonstrated that N and metal embedding significantly optimized the hydrogen adsorption on CNTs synergistically, and the introduction of Co was more efficient than the introduction of Fe which was consistent with the experimental results. As shown in Fig. 17a, strong H–C chemical bonding can be formed on the carbon surface of Fe@CNTs based on the band center of the occupied states of the C–H bond on Fe@CNTs locating in a low energy regime. Moreover, the reaction mechanism was also studied by DFT calculations (Fig. 17b and c), indicating that the Volmer–Heyrovsky mechanism was the predominant route in this catalytic system. In addition, to optimize the N content, FeCo alloy nanoparticles encapsulated in highly N-doped (8.2 atom%) graphene layers were synthesized,[130] which showed similar activity to the above FeCo@NCNTs. The DFT calculations showed that the N dopants could provide adsorption sites for H*, and the appropriate increase in N and the unique structure would decrease the ΔG_{H^*} for HER, thereby promoting the catalytic activity. Recently, a comprehensive understanding of FeCo coated with N–C was reported, based on theoretical calculations and experimental validations.[131] The effects of N-doping level and active N sites, the thickness of the carbon layers, and the binary alloying elements on catalytic activity were thoroughly analyzed, which should all be considered in synthesizing high-performance catalysts. FeCo@NC core–shell nanoparticles also displayed high OER activity with 10 mA cm^{-2} achieved at a potential of only 1.49 V in alkaline medium.[132]

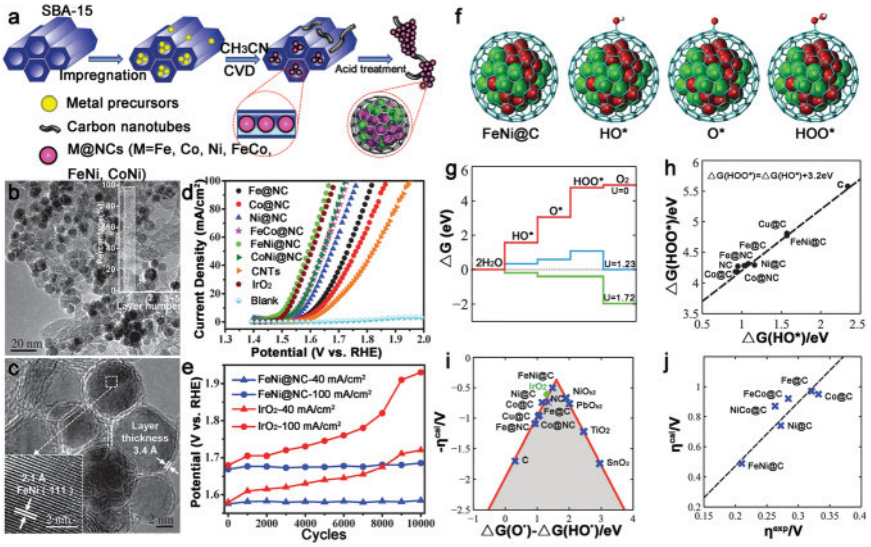

Fig. 16 (a) Schematic illustration of the synthesis process of M@NCs. (b and c) HRTEM images of FeNi@NC. The inset in (b) is a statistical analysis of the layer number of the graphene shell on metal nanoparticles. The inset in (c) shows the (111) crystal plane of the FeNi alloy and the graphene layer with a layer thickness of 3.4 Å. (d) OER polarization curves. (e) The potential changes in current densities at 40 mA cm^{-2} and 100 mA cm^{-2} for FeNi@NC and IrO_2 during the durability test. (f) The OER steps on the M@C models, where a graphitic carbon cage encapsulates 55 metal atoms. The grey cage, red and green balls represent C, Fe and Ni atoms, respectively. (g) Free energy profiles for the OER over FeNi@C at zero potential (U = 0), equilibrium potential for oxygen evolution (U = 1.23 V), and minimum potential (U = 1.72 V) where all steps run downhill. (h) Linear relation between the free energy of HO* and HOO* species on different catalysts. (i) The calculated negative overpotential against the universal descriptor ΔG(O*) − ΔG(HO*) on different catalysts. (j) Calculated overpotential *vs.* the experimental overpotential over M@C catalysts.

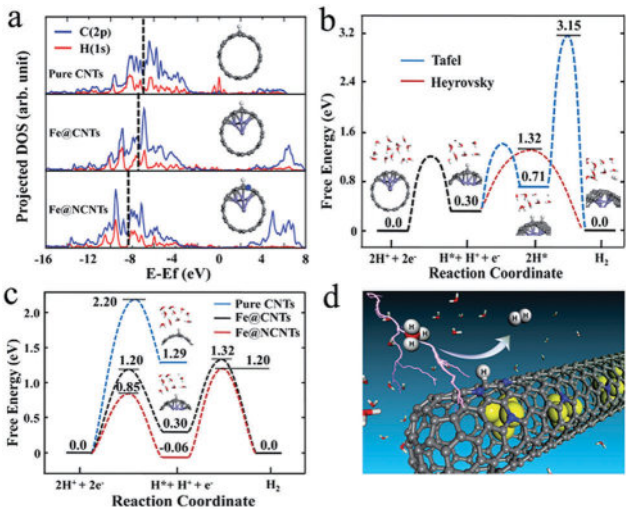

Fig. 17 (a) Comparison of projected density of states (DOS) of H (1s) and its bonded C (2p) when H is adsorbed on the surface of pristine CNTs, Fe@CNTs, and Fe@NCNTs. The dashed lines represent the center of the occupied band. (b) The free energy profiles of Tafel and Heyrovsky routes for Fe@CNTs. (c) The free energy profiles of the Heyrovsky route for pristine CNTs, Fe@CNTs and Fe@NCNTs. (d) A schematic representation of the HER process on the surface of Fe@NCNTs.

Alloy–N–C catalysts based on other alloy component have also been fabricated for water splitting. For instance, Zheng *et al.* synthesized NiMo encapsulated in N-graphite nanotubes (NiMo–NGTs) for HER in acid,[133] which exhibited high performance with an overpotential of only 65 mV at 10 mA cm^{-2} due to the synergetic effect of the Ni–Mo alloy and Mo_2C nanoparticles, as well as the NGT. However, the interaction between the metallic Ni phases and the Mo compound was not clear. Recently, Chen *et al.* also designed ternary alloys encapsulated in graphene for overall water splitting.[134] According to the DFT calculation, as for HER, the alloy with the most transferred electrons will exhibit the best HER performance. Whereas for OER, a proper number of transferred electrons which might result in an optimal value of ΔG(O*) − ΔG(HO*) in the volcano plot could enhance OER activity, which was similar to the previous report.[128] Thus, the change in alloy composition and proportion can further tune the surface electronic structures of carbon-encapsulated alloys by altering the number of transferred electrons to optimize the catalytic activity. In addition, the group also prepared an alloy of noble metal–N–C (PdCo@CN) catalyst for HER,[135] which showed outstanding performance with an overpotential of 80 mV at 10 mA cm^{-2}, a Tafel slope of 31 mV dec^{-1}, and excellent stability of 10 000 cycles.

5. Summary and outlook

In conclusion, this review has profiled several major kinds of M–N–C based materials for applications to electrochemical water splitting. A detailed comparison of their electrochemical performances was listed in Tables 1 and 2. We also briefly discussed the M–N–C structures and synthesis methods. The listed catalyst synthesis methods, including the precursors and treatment conditions, are summarized in Table 3. Based on the above experimental and theoretical results, we concluded that the synergistic effect of metal and N, as well as the carbon substrate contributed to the catalytic performance. Further study

Table 1 HER performance of some M–N–C catalysts

Catalysts	Electrolyte	Loading (mg cm^{-2})	Overpotential (mV)	Tafel slope (mA cm^{-2})	Exchange current density (mA cm^{-2})	Stability	Ref.
Co@NG	0.5 M H_2SO_4	1.08	η_{10} = 172	100	—	10 000 CV cycles	74
	1 M KOH		η_{10} = 200	112			
Co–NRCNTs	0.5 M H_2SO_4	0.28	η_{10} = 260	69	—	8.5 h	75
	phosphate buffer		η_{10} = 540	—			
	1 M KOH		η_{10} = 370	—			
Co@BCN	0.5 M H_2SO_4	—	η_{10} = 96	63.7	0.103	10 h	73
	1 M KOH		η_{10} = 183	73.2	—		
Co–NCNT/CC	0.5 M H_2SO_4	3.4	η_{10} = 78	74	0.38	40 h	78
	phosphate buffer		η_{10} = 170	97	—		
	1 M KOH		η_{10} = 180	193	—		
Co–N–GA	0.5 M H_2SO_4	0.28	η_{10} = 46	33	—	5000 CV cycles	79
	phosphate buffer		η_{10} = 299	159			
	1.0 M KOH		η_{10} = 232	102			
Co@Co–N–C	0.1 M KOH	—	η_{10} = 314	59	—	2000 CV cycles	76
Co@NC/NG	0.5 M H_2SO_4	0.285	$\eta_{13.6}$ = 200	79.3	—	1000 CV cycles	77
Co@NC/Ti	0.5 M H_2SO_4	11.2	η_{10} = 106	78.2	—	1000 CV cycles	80
Co–N–C	0.5 M H_2SO_4	0.765	η_{10} = 235	90	—	1000 CV cycles	81
Co–NC/NRGO	0.5 M H_2SO_4	0.35	η_{10} = 229	126	—	5000 CV cycles	91
Co–C–N/CFP	0.5 M H_2SO_4	—	η_{10} = 138	55	—	40 h	82
	phosphate buffer		η_{10} = 273	107			
	1.0 M KOH		η_{10} = 178	102			
CoN_x/C	0.5 M H_2SO_4	2.0	η_{10} = 133	57	0.07	5000 CV cycles	83
	phosphate buffer		η_{10} = 247	—	—		
	1.0 M KOH		η_{10} = 170	75	—		
CoNC/GD	0.5 M H_2SO_4	0.256	η_{10} = 340	138	—	38 000 CV cycles	106
	phosphate buffer		η_{10} = 368	207		9000 CV cycles	
	1.0 M KOH		η_{10} = 284	115		36 000 CV cycles	
Co@N–C	1 M $HClO_4$	—	η_{10} = 200	100	—	10 000 CV cycles	94
	1 M KOH		η_{10} = 210	108			
Co–NC/CNT	1 M KOH	0.306	η_{10} = 203	125	—	1000 CV cycles	95
Co@NCNT	0.5 M H_2SO_4	—	η_{10} = 210	93	—	20 000 s	96
CoO_x@CN	1 M KOH	0.12	η_{10} = 232	115	—	—	97
Co–P/NC	1 M KOH	1	η_{10} = 154	51	—	1000 CV cycles	107
Co–P/NC/CC	1 M KOH	—	η_{10} = 171	52	—	—	108
Co–NG	0.5 M H_2SO_4	0.285	η_{10} = 147	82	—	10 h	98
Ni–C–N	0.5 M H_2SO_4	0.2	η_{10} = 60.9	32	0.0136	70 h	109
	phosphate buffer		η_{10} = 92.1	38	—		
	1 M KOH		η_{10} = 30.8	40	—		
A–Ni–C	0.5 M H_2SO_4	0.283	η_{10} = 34	41	1.2	25 h	111
Fe_3C/Mo_2C@NPGC	0.5 M H_2SO_4	—	η_{10} = 98	45.2	0.104	10 h	118
Au@NC	0.5 M H_2SO_4	0.357	η_{10} = 130	76.8	0.186	20 h	121
Pt/NGNs	0.5 M H_2SO_4	0.076	η_{16} = 50	29	—	1000 CV cycles	126
CoNi@NC	0.1 M H_2SO_4	0.32	η_{10} = 224	104	—	24 h	127
FeCo@NCNTs	0.1 M H_2SO_4	0.32	η_{onset} = 70	74	—	10 000 CV cycles	113
FeCo@N–GR	0.5 M H_2SO_4	0.285	η_{10} = 262	74	—	10 000 CV cycles	130
FeCo@NC	0.5 M H_2SO_4	—	η_{10} = 240	92	—	10 000 CV cycles	131
NiMo–NGTs	0.5 M H_2SO_4	2	η_{10} = 65	67	0.84	10 000 CV cycles	133
PdCo@CN	0.5 M H_2SO_4	0.285	η_{10} = 80	31	—	10 000 CV cycles	135

also demonstrated that the different metals, N contents and the carbon layer thickness all had significance effects on the activity. In addition, the experimental solar cell devices using these catalysts made a further step towards environmentally friendly hydrogen production.

Despite these meaningful conclusions, several challenges still remain. (i) The limit of synthesis methods leads to many adverse effects. For instance, during the general pyrolysis process, many factors, such as temperature and gas flow rate, give products poor reproducibility. Thus, it is hard to move on to large-scale production and the precise composition control of catalyst materials. Furthermore, the controllable synthesis of catalysts with a large effective surface area and a high density of catalytic active sites are seldom achieved at the same time. (ii) The atomic structure and catalytic mechanism of the M–N–C catalysts are still hard to illustrate clearly, due to the complex nature of these catalysts. So the nature of the real active sites in M–N–C composites for water electrolysis remains a topic of controversy, which goes against effective catalyst design and causes great puzzlement in the further understanding of these reactions.

The rapid development of M–N–C catalysts for water splitting always results in insufficient understanding. Nowadays, many researchers focus on preparing M–N–C catalysts with different components and then characterize their electrochemical performance. More attention should be paid to the mechanistic and fundamental insights of M–N–C catalysts in the water electrolysis process. Some future directions are now discussed, which

Table 2 OER performance of some M–N–C catalysts

Catalysts	Electrolyte	Loading (mg cm^{-2})	Overpotential (mV)	Tafel slope (mA cm^{-2})	Stability	Ref.
Co–N–CNTs	Phosphate buffer	1.0	η_{10} = 300	50	6 h	84
	1.0 M KOH		η_{50} = 300	40		
Co–N–GCI	0.1 M KOH	0.5	η_{10} = 426	—	200 CV cycles	85
Co@Co_3O_4/NC	0.1 M KOH	0.21	η_{10} = 410	53	45 h	86
Co–N–C	0.1 M KOH	0.4	η_{10} = 390	110	10 h	88
Co/N–C	0.1 M KOH	0.25	η_{10} = 371	61.4	500 CV cycles	89
Co–NC/NRGO	0.1 M KOH	0.35	η_{10} = 430	292	6000 s	91
Co@N–C	1.0 M KOH	—	η_{10} = 400	—	550 min	94
Co–NC/CNT	1.0 M KOH	0.306	η_{10} = 354	78	1000 CV cycles	95
Co@NCNT	1.0 M KOH	—	η_{10} = 429	116	—	96
CoO_x@CN	1.0 M KOH	1	η_{10} = 260	—	—	97
Co–P/NC	1.0 M KOH	1	η_{10} = 319	52	1000 CV cycles	107
Co–P/NC/CC	1.0 M KOH	—	η_{10} = 330	61	50 h	108
Ni@NC	0.1 M KOH	0.4	η_{10} = 390	40	10 h	112
Fe–N–C	0.1 M KOH	0.6	η_{10} = 370	82	—	115
Fe_3C@NCNT/NPC	1.0 M KOH	—	η_{10} = 340	62	1000 CV cycles	116
FeNC	0.1 M KOH	0.15	η_{10} = 410	137	5000 s	117
FeNi@NC	1.0 M NaOH	0.32	η_{10} = 280	70	10 000 CV cycles	128
NiFe@NC_x	0.1 M KOH	0.4	η_{10} = 230	60.6	1000 CV cycles	129
FeCo@NC	1.0 M KOH	0.8	η_{10} = 260	62	6 h	131
FeCoNi/N–GR	1.0 M KOH	1	η_{10} = 288	60	1000 CV cycles	134

Table 3 Synthesis process of the above M–N–C catalysts

Catalysts[ref.]	Precursors	Synthesis conditions
Co@BCN[73]	ZIF-67 and H_3BO_3	Calcination at 450 °C in Ar atmosphere, then increased to 750 °C
Co@NG[74]	Co-containing prussian blue colloids	Annealed in Ar at 600 °C for 1 h and then acid treatment
Co–NRCNTs[75]	Dicyandiamide and $CoCl_2{\cdot}6H_2O$	Thermal treatment at 500 and 700 °C in N_2 atmosphere, and then acid treatment
Co@Co–N–C[76]	$Co(OH)(CO_3)_{0.5}{\cdot}0.11H_2O$@polymerized glucose and melamine	Calcination in Ar atmosphere at 800 °C for 2 h
Co@NC/NG[77]	$Co(Ac)_2{\cdot}4H_2O$, cyanamide, graphene oxide	Thermal treatment at 500 and 700 °C in N_2 atmosphere for 2 h, followed by acid treatment
Co–NCNT/CC[78]	Dicyanodiamine and Co_3O_4/CC	Calcination at 400 and 700 °C for 2 h, respectively, and then acid treatment
Co–N–GA[79]	MOFs@graphene	Pyrolysis at 900 °C for 2 h in Ar atmosphere
Co@NC/Ti[80]	Co_3O_4/Ti and dicyanodiamine	Calcination at 700 °C in Ar atmosphere
Co–N–C[81]	$Co(NO_3)_2{\cdot}6H_2O$, aniline and carbon black	Treatment at 900 °C in Ar atmosphere for 1 h, and then acid treatment
Co–C–N/CFP[82]	$Co(NO_3)_2{\cdot}6H_2O$ and polyaniline	Carbonized at 750 °C in N_2 atmosphere, and then acid treatment
CoN_x/C[83]	Co/*o*-phenylenediamine	Pyrolysis at 900 °C under N_2 atmosphere for 2 h, alkali treatment, second heat treatment, acid treatment, third heat treatment
Co–N–CNTs[84]	Co-phthalocyanine and carbon nanotube	Heated at 900 °C for 2 h in Ar, and then acid treatment
Co–N–GCI[85]	$Co(Ac)_2{\cdot}4H_2O$, melamine and carbon nanospheres	Thermal treatment at 750 °C for 30 min under Ar flow
Co@Co_3O_4/NC[86]	ZIF-67	Pyrolysis in H_2 atmosphere and subsequent controlled oxidative calcination
Co–N/C[87]	$CoCl_2{\cdot}6H_2O$, hdatrz and carbon black	Thermal-treated at 600 °C for 2 h under N_2 atmosphere
Co–N–C[88]	$Co(Ac)_2{\cdot}4H_2O$ and g-C_3N_4	Calcination at 500 °C 2 h and 700 °C for 4 h under N_2 atmosphere, respectively, and then acid treatment, 800 °C again in N_2 atmosphere for 2 h
Co/N–C[89]	$Co(Ac)_2{\cdot}4H_2O$ and dopamine hydrochloride	Thermal-treated at 800 °C for 2 h under Ar atmosphere
Co/N–C[90]	Dikaryon phthalocyanine Co sulfonate	Pyrolysis at 900 °C and constant pressure of 1.5 Torr for 2 h under N_2 atmosphere
Co–NC/NRGO[91]	ZIF-67 and graphene oxide	Thermally treated under flowing Ar at 900 °C and then acid treatment
Co/CoO@Co–N–C[92]	$Co(NO_3)_2$, N-doped carbon nanodots and pyrrole	Thermal-treated at 800 °C for 2 h under N_2 atmosphere
Co@N–C[94]	$Co(Ac)_2{\cdot}4H_2O$ and imidazole	Pyrolysis at 900 °C in Ar atmosphere for 2 h, acid treatment, 900 °C again in Ar atmosphere for 1 h
Co–NC/CNT[95]	ZIF-67 and CNTs	Pyrolysis at 800 °C under N_2 flow for 2 h and acid treatment
Co@NCNT[96]	ZIF-67 and dicyandiamide	Calcination at 500 °C 30 min and 750 °C for 2 h under flowing Ar, and then acid treatment
CoO_x@CN[97]	$CoNO_3{\cdot}6H_2O$, melamine and D(+)-glucosamine hydrochloride	Calcination at 600 °C 1 h and 800 °C for 1 h in N_2 atmosphere, respectively
Co–NG[98]	$CoCl_2{\cdot}6H_2O$ and graphene oxide	Calcination at 750 °C for 1 h under NH_3 atmosphere
CoNC/GD[106]	$Co(oAc)_2$, DCD and GD	Calcination at 500 °C 2 h and 700 °C for 2 h in Ar atmosphere, and then acid treatment
Co–C_3N_4/CNT[122]	$CoCl_2{\cdot}6H_2O$, CNT and DCDA	Thermal-treated at 600 °C under N_2 atmosphere
Co–P/NC[107]	ZIF-67 and $NaH_2PO_2{\cdot}H_2O$	Carbonization of ZIF-67 followed by phosphidation
Co–P/NC/CC[108]	ZIF-67/CC and $NaH_2PO_2{\cdot}H_2O$	Carbonization of ZIF-67/CC followed by phosphidation

Table 3 (*continued*)

Catalysts[ref.]	Precursors	Synthesis conditions
Ni–C–N[109]	Ni–polyoxometalate MOF	Carbonization Ni–MOF in NH_3 atmosphere at 380 °C for 3 h, acid treatment, followed by exfoliation
A–Ni–C[111]	Ni–MOF	Carbonization at 700 °C in N_2 atmosphere, and then treatment
Ni@NC[112]	$Ni(Ac)_2$ and phenanthroline	Carbonization at 800 °C under N_2 flow for 1.5 h
Fe–N–C[114]	Fe phthalocyanine	Carbonized at 900 °C for 3 h under Ar atmosphere
Fe–N–C[115]	CNTs with 2,2-bipyridine and $FeCl_3$	Pyrolysis at 900 °C under N_2 atmosphere and acid leaching
Fe_3C@NCNT/NPC[116]	MIL-88B and melamine	Calcination at 550 °C 3 h and 800 °C for 2 h in N_2 atmosphere, respectively, and then acid treatment
FeNC[117]	$FeCl_3$, *o*-phthalic anhydride, and melamine	Calcination at 550 °C 3 h and 800 °C for 2 h in N_2 atmosphere, and then acid treatment
Fe_3C/Mo_2C@NPGC[118]	PMo_{12}@MIL-100 (Fe) and melamine	Pyrolysis at 900 °C under N_2 atmosphere
CoNi@NC[127]	$Co(NO_3)_2$, $Ni(NO_3)_2$, and Na_4EDTA	Annealed at a temperature range of 425 to 600 °C for 3 h in Ar, and then acid treatment
NiFe@NC_x[129]	NiFe-MILs and melamine	Calcination at 600 °C for 1 h and 800 °C for 1 h in N_2 atmosphere, and then acid treatment
FeCo@N–GR[130]	$Fe_3[Co(CN)_6]_2$	Annealing of MOF nanoparticles at 600 °C in N_2
FeCo@NC[131]	$Fe(NO_3)_3{\cdot}9H_2O$, $Co(NO_3)_2{\cdot}6H_2O$, glucose and ammonium sulfate	Pyrolysis at 1000 °C, acid treatment and treated again at 1000 °C for 1 h under Ar flow
FeCo@NC[132]	Co–Fe prussian blue analogue	Thermal decomposition in Ar atmosphere
NiMo–NGTs[133]	$Ni(Ac)_2{\cdot}4H_2O$, dicyandiamide $(NH_4)_6Mo_7O_{24}{\cdot}4H_2O$	Calcination at 600 °C 2 h in a 5 : 2 Ar/H_2 (v/v) atmosphere
FeCoNi/N–GR[134]	$Fe_3[Co(CN)_6]_2$ and $Ni_3[Co(CN)_6]_2$	Annealed under N_2 atmosphere at 600 °C for 4 h
PdCo@CN[135]	Pd-Doped MOFs	Annealed under N_2 atmosphere at 500 °C for 4 h

may be expanded to other systems. (i) The best catalytic performance is still far from the expectations for practical applications, which should lead to further improvement. The catalytic performance can be further enhanced by optimizing the M–N binding properties and catalyst structures with a large effective surface area and a high density of catalytic active sites, as well as the relationships between metal, carbon layers and N-doping level, and even heteroatom doping, *etc.* In addition, the metal and/or its oxide, carbide, nitride and phosphide, and even other coordinated atoms, such as molecular M–S_x and M–P_x, should be considered. Moreover, other carbon matrixes, such as the above-mentioned graphdiyne and g-C_3N_4 should be also designed and studied. (ii) Theoretical calculation is a powerful technology to illustrate many profound questions, such as the effect of crystal structure, heteroatom doping and electronic state. These theories, combined with the above factors, can help us gain deep insight into the mechanism, and then guide us in designing and optimizing M–N–C catalysts with high performance. (iii) Considering practical applications, fabricating integrated bifunctional electrodes with special structures in the same electrolyte for water electrolysis should be also considered. Integrated electrodes can avoid not only time- and cost-consuming processes, but also the disadvantages of using polymer binders, such as increasing series resistance, blocking active sites and inhibiting diffusion. And working in the same electrolyte allows a simpler design of electrolyzer systems. Also, a combination of these catalysts with solar cell devices should be tried, and only a few workers focus on this. (iv) A lack of understanding of the molecular-level interfacial structural transformation and reaction mechanisms will always hinder the further development of this thriving field. Once acquired, a new comprehensive understanding in this area by advanced *in situ* characterization techniques, will be another big step towards electrochemical water splitting.

Acknowledgements

This work was supported by National Natural Science Foundation of China (51522101, 51471075, 5163100, and 51401084); and Specialized Research Fund for the Doctoral Program of Higher Education of China (20110061120040).

Notes and references

1 Y. Yan, B. Y. Xia, Z. C. Xu and X. Wang, *ACS Catal.*, 2014, **4**, 1693–1705.
2 T. R. Cook, D. K. Dogutan, S. Y. Reece, Y. Surendranath, T. S. Teets and D. G. Nocera, *Chem. Rev.*, 2010, **110**, 6474–6502.
3 M. G. Walter, E. L. Warren, J. R. McKone, S. W. Boettcher, Q. Mi, E. A. Santori and N. S. Lewis, *Chem. Rev.*, 2010, **110**, 6446–6473.
4 Z. W. Seh, J. Kibsgaard, C. F. Dickens, I. Chorkendorff, J. K. Norskov and T. F. Jaramillo, *Science*, 2017, 355.
5 L. M. Amoo and R. L. Fagbenle, *Int. J. Hydrogen Energy*, 2014, **39**, 12409–12433.
6 J. A. Turner, *Science*, 2004, **305**, 972–974.
7 X. Zou and Y. Zhang, *Chem. Soc. Rev.*, 2015, **44**, 5148–5180.
8 J. Wang, W. Cui, Q. Liu, Z. Xing, A. M. Asiri and X. Sun, *Adv. Mater.*, 2016, **28**, 215–230.
9 A. Kudo and Y. Miseki, *Chem. Soc. Rev.*, 2009, **38**, 253–278.
10 V. S. Thoi, Y. Sun, J. R. Long and C. J. Chang, *Chem. Soc. Rev.*, 2013, **42**, 2388–2400.
11 T. Abbasi and S. A. Abbasi, *Renewable Sustainable Energy Rev.*, 2011, **15**, 3034–3040.
12 M. Wang, Z. Wang, X. Gong and Z. Guo, *Renewable Sustainable Energy Rev.*, 2014, **29**, 573–588.
13 J. A. Turner, *Science*, 1999, **285**, 687–689.
14 J. Wang, H.-X. Zhong, Z.-L. Wang, F.-L. Meng and X.-B. Zhang, *ACS Nano*, 2016, **10**, 2342–2348.

15 D. Voiry, H. Yamaguchi, J. Li, R. Silva, D. C. B. Alves, T. Fujita, M. Chen, T. Asefa, V. B. Shenoy, G. Eda and M. Chhowalla, *Nat. Mater.*, 2013, **12**, 850–855.
16 T. Y. Ma, J. Ran, S. Dai, M. Jaroniec and S. Z. Qiao, *Angew. Chem., Int. Ed.*, 2015, **54**, 4646–4650.
17 Y. Zheng, Y. Jiao, M. Jaroniec and S. Z. Qiao, *Angew. Chem., Int. Ed.*, 2015, **54**, 52–65.
18 P. Jiang, Q. Liu, Y. Liang, J. Tian, A. M. Asiri and X. Sun, *Angew. Chem., Int. Ed.*, 2014, **53**, 12855–12859.
19 J. Q. Tian, Q. Liu, A. M. Asiri and X. P. Sun, *J. Am. Chem. Soc.*, 2014, **136**, 7587–7590.
20 J.-S. Li, Y. Wang, C.-H. Liu, S.-L. Li, Y.-G. Wang, L.-Z. Dong, Z.-H. Dai, Y.-F. Li and Y.-Q. Lan, *Nat. Commun.*, 2016, **7**, 11204.
21 W. Liu, E. Hu, H. Jiang, Y. Xiang, Z. Weng, M. Li, Q. Fan, X. Yu, E. I. Altman and H. Wang, *Nat. Commun.*, 2016, **7**, 10771.
22 Y. Jiao, Y. Zheng, K. Davey and S.-Z. Qiao, *Nat. Energy*, 2016, **1**, 16130.
23 H. Zhong, J. Wang, F. Meng and X. Zhang, *Angew. Chem., Int. Ed.*, 2016, **55**, 9937–9941.
24 M. Gong, Y. Li, H. Wang, Y. Liang, J. Z. Wu, J. Zhou, J. Wang, T. Regier, F. Wei and H. Dai, *J. Am. Chem. Soc.*, 2013, **135**, 8452–8455.
25 T. Y. Ma, S. Dai, M. Jaroniec and S. Z. Qiao, *J. Am. Chem. Soc.*, 2014, **136**, 13925–13931.
26 X. Lu and C. Zhao, *Nat. Commun.*, 2015, **6**, 6616.
27 J. Liang, R. F. Zhou, X. M. Chen, Y. H. Tang and S. Z. Qiao, *Adv. Mater.*, 2014, **26**, 6074–6079.
28 L. Dai, Y. Xue, L. Qu, H.-J. Choi and J.-B. Baek, *Chem. Rev.*, 2015, **115**, 4823–4892.
29 Y. Nie, L. Li and Z. Wei, *Chem. Soc. Rev.*, 2015, **44**, 2168–2201.
30 T. Zhou, Y. Du, S. Yin, X. Tian, H. Yang, X. Wang, B. Liu, H. Zheng, S. Qiao and R. Xu, *Energy Environ. Sci.*, 2016, **9**, 2563–2570.
31 G. Wu, K. L. More, C. M. Johnston and P. Zelenay, *Science*, 2011, **332**, 443–447.
32 Z. Dong, H. Ren, C. M. Hessel, J. Wang, R. Yu, Q. Jin, M. Yang, Z. Hu, Y. Chen, Z. Tang, H. Zhao and D. Wang, *Adv. Mater.*, 2014, **26**, 905–909.
33 J. Wang, H. Tang, H. Ren, R. Yu, J. Qi, D. Mao, H. Zhao and D. Wang, *Adv. Sci.*, 2014, **1**, 1400011.
34 J. Wang, N. Yang, H. Tang, Z. Dong, Q. Jin, M. Yang, D. Kisailus, H. Zhao, Z. Tang and D. Wang, *Angew. Chem., Int. Ed.*, 2013, **52**, 6417–6420.
35 J. Qi, X. Lai, J. Wang, H. Tang, H. Ren, Y. Yang, Q. Jin, L. Zhang, R. Yu, G. Ma, Z. Su, H. Zhao and D. Wang, *Chem. Soc. Rev.*, 2015, **44**, 6749–6773.
36 S. Xu, C. M. Hessel, H. Ren, R. Yu, Q. Jin, M. Yang, H. Zhao and D. Wang, *Energy Environ. Sci.*, 2014, **7**, 632–637.
37 J. Zhang, H. Ren, J. Wang, J. Qi, R. Yu, D. Wang and Y. Liu, *J. Mater. Chem. A*, 2016, **4**, 17673–17677.
38 J. Wang, H. Tang, H. Wang, R. Yu and D. Wang, *Mater. Chem. Front.*, 2017, **1**, 414–430.
39 H. Ren, R. Yu, J. Wang, Q. Jin, M. Yang, D. Mao, D. Kisailus, H. Zhao and D. Wang, *Nano Lett.*, 2014, **14**, 6679–6684.
40 J. Qi, K. Zhao, G. Li, Y. Gao, H. Zhao, R. Yu and Z. Tang, *Nanoscale*, 2014, **6**, 4072–4077.
41 J. Wang, H. Tang, L. Zhang, H. Ren, R. Yu, Q. Jin, J. Qi, D. Mao, M. Yang, Y. Wang, P. Liu, Y. Zhang, Y. Wen, L. Gu, G. Ma, Z. Su, Z. Tang, H. Zhao and D. Wang, *Nat. Energy*, 2016, **1**, 16050.
42 C. G. Morales-Guio, L. A. Stern and X. L. Hu, *Chem. Soc. Rev.*, 2014, **43**, 6555–6569.
43 Y. Shi and B. Zhang, *Chem. Soc. Rev.*, 2016, **45**, 1529–1541.
44 M. Zeng and Y. Li, *J. Mater. Chem. A*, 2015, **3**, 14942–14962.
45 R. Jasinski, *Nature*, 1964, **201**, 1212.
46 M. Zhou, C. Z. Yang and K. Y. Chan, *Adv. Energy Mater.*, 2014, **4**, 1400840.
47 M. Xiao, J. Zhu, L. Feng, C. Liu and W. Xing, *Adv. Mater.*, 2015, **27**, 2521–2527.
48 Y. Hu, J. O. Jensen, W. Zhang, L. N. Cleemann, W. Xing, N. J. Bjerrum and Q. Li, *Angew. Chem., Int. Ed.*, 2014, **53**, 3675–3679.
49 U. Tylus, Q. Jia, K. Strickland, N. Ramaswamy, A. Serov, P. Atanassov and S. Mukerjee, *J. Phys. Chem. C*, 2014, **118**, 8999–9008.
50 K. Shen, X. Chen, J. Chen and Y. Li, *ACS Catal.*, 2016, **6**, 5887–5903.
51 S. Ganesan, N. Leonard and S. C. Barton, *Phys. Chem. Chem. Phys.*, 2014, **16**, 4576–4585.
52 M. Lefevre, J. P. Dodelet and P. Bertrand, *J. Phys. Chem. B*, 2000, **104**, 11238–11247.
53 U. I. Kramm, J. Herranz, N. Larouche, T. M. Arruda, M. Lefevre, F. Jaouen, P. Bogdanoff, S. Fiechter, I. Abs-Wurmbach, S. Mukerjee and J. P. Dodelet, *Phys. Chem. Chem. Phys.*, 2012, **14**, 11673–11688.
54 A. Zitolo, V. Goellner, V. Armel, M. T. Sougrati, T. Mineva, L. Stievano, E. Fonda and F. Jaouen, *Nat. Mater.*, 2015, **14**, 937–942.
55 W. Liu, L. Zhang, W. Yan, X. Liu, X. Yang, S. Miao, W. Wang, A. Wang and T. Zhang, *Chem. Sci.*, 2016, **7**, 5758–5764.
56 A. Mahmood, W. Guo, H. Tabassum and R. Zou, *Adv. Energy Mater.*, 2016, **6**, 1600423.
57 Z.-F. Ma, X.-Y. Xie, X.-X. Ma, D.-Y. Zhang, Q. Ren, N. Heß-Mohr and V. M. Schmidt, *Electrochem. Commun.*, 2006, **8**, 389–394.
58 H. Liu, C. Song, Y. Tang, J. Zhang and J. Zhang, *Electrochim. Acta*, 2007, **52**, 4532–4538.
59 F. Jaouen, F. Charreteur and J. P. Dodelet, *J. Electrochem. Soc.*, 2006, **153**, A689.
60 M. Lefevre, E. Proietti, F. Jaouen and J.-P. Dodelet, *Science*, 2009, **324**, 71–74.
61 D. Deng, L. Yu, X. Chen, G. Wang, L. Jin, X. Pan, J. Deng, G. Sun and X. Bao, *Angew. Chem., Int. Ed.*, 2013, **52**, 371–375.
62 H. Xiao, Z.-G. Shao, G. Zhang, Y. Gao, W. Lu and B. Yi, *Carbon*, 2013, **57**, 443–451.
63 J.-S. Lee, G. S. Park, S. T. Kim, M. Liu and J. Cho, *Angew. Chem., Int. Ed.*, 2013, **52**, 1026–1030.
64 K. Ai, Y. Liu, C. Ruan, L. Lu and G. M. Lu, *Adv. Mater.*, 2013, **25**, 998–1003.

65 G. Wu, C. M. Johnston, N. H. Mack, K. Artyushkova, M. Ferrandon, M. Nelson, J. S. Lezama-Pacheco, S. D. Conradson, K. L. More, D. J. Myers and P. Zelenay, *J. Mater. Chem.*, 2011, **21**, 11392.
66 A. Kong, X. Zhu, Z. Han, Y. Yu, Y. Zhang, B. Dong and Y. Shan, *ACS Catal.*, 2014, **4**, 1793–1800.
67 F. L. Meng, Z. L. Wang, H. X. Zhong, J. Wang, J. M. Yan and X. B. Zhang, *Adv. Mater.*, 2016, **28**, 7948–7955.
68 Y. V. Kaneti, J. Tang, R. R. Salunkhe, X. Jiang, A. Yu, K. C. Wu and Y. Yamauchi, *Adv. Mater.*, 2017, **29**, 1604898.
69 Z. Tao, T. Wang, X. Wang, J. Zheng and X. Li, *ACS Appl. Mater. Interfaces*, 2016, **8**, 35390–35397.
70 K. Shen, L. Chen, J. Long, W. Zhong and Y. Li, *ACS Catal.*, 2015, **5**, 5264–5271.
71 E. Proietti, F. Jaouen, M. Lefevre, N. Larouche, J. Tian, J. Herranz and J. P. Dodelet, *Nat. Commun.*, 2011, **2**, 416.
72 S. Chen, J. Duan, J. Ran, M. Jaroniec and S. Z. Qiao, *Energy Environ. Sci.*, 2013, **6**, 3693–3699.
73 H. Zhang, Z. Ma, J. Duan, H. Liu, G. Liu, T. Wang, K. Chang, M. Li, L. Shi, X. Meng, K. Wu and J. Ye, *ACS Nano*, 2016, **10**, 684–694.
74 M. Zeng, Y. Liu, F. Zhao, K. Nie, N. Han, X. Wang, W. Huang, X. Song, J. Zhong and Y. Li, *Adv. Funct. Mater.*, 2016, **26**, 4397–4404.
75 X. C. Zou, X. C. Huang, A. Goswami, R. Silva, B. R. Sathe, E. Mikmekova and T. Asefa, *Angew. Chem., Int. Ed.*, 2014, **53**, 4372–4376.
76 Y. Wang, Y. Nie, W. Ding, S. G. Chen, K. Xiong, X. Q. Qi, Y. Zhang, J. Wang and Z. D. Wei, *Chem. Commun.*, 2015, **51**, 8942–8945.
77 W. Zhou, J. Zhou, Y. Zhou, J. Lu, K. Zhou, L. Yang, Z. Tang, L. Li and S. Chen, *Chem. Mater.*, 2015, **27**, 2026–2032.
78 Z. Xing, Q. Liu, W. Xing, A. M. Asiri and X. Sun, *ChemSusChem*, 2015, **8**, 1850–1855.
79 Z. Zhu, Y. Yang, Y. Guan, J. Xue and L. Cui, *J. Mater. Chem. A*, 2016, **4**, 15536–15545.
80 W. Zhou, Y. Zhou, L. Yang, J. Huang, Y. Ke, K. Zhou, L. Li and S. Chen, *J. Mater. Chem. A*, 2015, **3**, 1915–1919.
81 L. Zhang, W. Liu, Y. Dou, Z. Du and M. Shao, *J. Phys. Chem. C*, 2016, **120**, 29047–29053.
82 Z.-L. Wang, X.-F. Hao, Z. Jiang, X.-P. Sun, D. Xu, J. Wang, H.-X. Zhong, F.-L. Meng and X.-B. Zhang, *J. Am. Chem. Soc.*, 2015, **137**, 15070–15073.
83 H.-W. Liang, S. Brueller, R. Dong, J. Zhang, X. Feng and K. Muellen, *Nat. Commun.*, 2015, **6**, 7992.
84 Z. Wang, S. Xiao, Z. Zhu, X. Long, X. Zheng, X. Lu and S. Yang, *ACS Appl. Mater. Interfaces*, 2015, **7**, 4048–4055.
85 X. Qiao, S. Liao, R. Zheng, Y. Deng, H. Song and L. Du, *ACS Sustainable Chem. Eng.*, 2016, **4**, 4131–4136.
86 A. Aijaz, J. Masa, C. Rosler, W. Xia, P. Weide, A. J. Botz, R. A. Fischer, W. Schuhmann and M. Muhler, *Angew. Chem., Int. Ed.*, 2016, **55**, 4087–4091.
87 S. Chao and M. Geng, *Int. J. Hydrogen Energy*, 2016, **41**, 12995–13004.
88 Y. Hu, E. Hu, J. Ning, B. He, Z. Li, C. C. Zheng, Y. Zhong and Z. Zhang, *J. Mater. Chem. A*, 2017, **5**, 2271–2279.
89 Y. Su, Y. Zhu, H. Jiang, J. Shen, X. Yang, W. Zou, J. Chen and C. Li, *Nanoscale*, 2014, **6**, 15080–15089.
90 S. Guo, Y. Yang, N. Liu, S. Qiao, H. Huang, Y. Liu and Z. Kang, *Sci. Bull.*, 2016, **61**, 68–77.
91 Y. Hou, Z. Wen, S. Cui, S. Ci, S. Mao and J. Chen, *Adv. Funct. Mater.*, 2015, **25**, 872–882.
92 X. Zhang, R. Liu, Y. Zang, G. Liu, G. Wang, Y. Zhang, H. Zhang and H. Zhao, *Chem. Commun.*, 2016, **52**, 5946–5949.
93 X. Li, Z. Niu, J. Jiang and L. Ai, *J. Mater. Chem. A*, 2016, **4**, 3204–3209.
94 J. Wang, D. Gao, G. Wang, S. Miao, H. Wu, J. Li and X. Bao, *J. Mater. Chem. A*, 2014, **2**, 20067–20074.
95 F. Yang, P. Zhao, X. Hua, W. Luo, G. Cheng, W. Xing and S. Chen, *J. Mater. Chem. A*, 2016, **4**, 16057–16063.
96 E. Zhang, Y. Xie, S. Ci, J. Jia, P. Cai, L. Yi and Z. Wen, *J. Mater. Chem. A*, 2016, **4**, 17288–17298.
97 H. Jin, J. Wang, D. Su, Z. Wei, Z. Pang and Y. Wang, *J. Am. Chem. Soc.*, 2015, **137**, 2688–2694.
98 H. Fei, J. Dong, M. J. Arellano-Jimenez, G. Ye, N. Dong Kim, E. L. Samuel, Z. Peng, Z. Zhu, F. Qin, J. Bao, M. J. Yacaman, P. M. Ajayan, D. Chen and J. M. Tour, *Nat. Commun.*, 2015, **6**, 8668.
99 D. W. Ma, T. Li, Q. Wang, G. Yang, C. He, B. Ma and Z. Lu, *Carbon*, 2015, **95**, 756–765.
100 Y. Li, L. Xu, H. Liu and Y. Li, *Chem. Soc. Rev.*, 2014, **43**, 2572–2586.
101 A. H. Mashhadzadeh, A. M. Vahedi, M. Ardjmand and M. G. Ahangari, *Superlattices Microstruct.*, 2016, **100**, 1094–1102.
102 X. Gao, J. Li, R. Du, J. Zhou, M. Y. Huang, R. Liu, J. Li, Z. Xie, L. Z. Wu, Z. Liu and J. Zhang, *Adv. Mater.*, 2017, **29**, 1605308.
103 H. Ren, H. Shao, L. Zhang, D. Guo, Q. Jin, R. Yu, L. Wang, Y. Li, Y. Wang, H. Zhao and D. Wang, *Adv. Energy Mater.*, 2015, **5**, 1500296.
104 J. Li, X. Gao, B. Liu, Q. Feng, X. B. Li, M. Y. Huang, Z. Liu, J. Zhang, C. H. Tung and L. Z. Wu, *J. Am. Chem. Soc.*, 2016, **138**, 3954–3957.
105 Y. Xue, Y. Guo, Y. Yi, Y. Li, H. Liu, D. Li, W. Yang and Y. Li, *Nano Energy*, 2016, **30**, 858–866.
106 Y. Xue, J. Li, Z. Xue, Y. Li, H. Liu, D. Li, W. Yang and Y. Li, *ACS Appl. Mater. Interfaces*, 2016, **8**, 31083–31091.
107 B. You, N. Jiang, M. Sheng, S. Gul, J. Yano and Y. Sun, *Chem. Mater.*, 2015, **27**, 7636–7642.
108 X. Liu, J. Dong, B. You and Y. Sun, *RSC Adv.*, 2016, **6**, 73336–73342.
109 J. Yin, Q. Fan, Y. Li, F. Cheng, P. Zhou, P. Xi and S. Sun, *J. Am. Chem. Soc.*, 2016, **138**, 14546–14549.
110 Z. Chen, Z. Ma, J. Song, L. Wang and G. Shao, *J. Power Sources*, 2016, **324**, 86–96.
111 L. Fan, P. F. Liu, X. Yan, L. Gu, Z. Z. Yang, H. G. Yang, S. Qiu and X. Yao, *Nat. Commun.*, 2016, **7**, 10667.
112 J. Ren, M. Antonietti and T.-P. Fellinger, *Adv. Energy Mater.*, 2015, **5**, 1401660.
113 J. Deng, P. J. Ren, D. H. Deng, L. Yu, F. Yang and X. H. Bao, *Energy Environ. Sci.*, 2014, **7**, 1919–1923.

114 M. Y. Song, D.-S. Yang, K. P. Singh, J. Yuan and J.-S. Yu, *Appl. Catal., B*, 2016, **191**, 202–208.
115 P. Chen, T. Zhou, L. Xing, K. Xu, Y. Tong, H. Xie, L. Zhang, W. Yan, W. Chu, C. Wu and Y. Xie, *Angew. Chem., Int. Ed.*, 2017, **56**, 610–614.
116 P. Zhao, X. Hua, W. Xu, W. Luo, S. Chen and G. Cheng, *Catal. Sci. Technol.*, 2016, **6**, 6365–6371.
117 P. Zhao, W. Xu, X. Hua, W. Luo, S. Chen and G. Cheng, *J. Phys. Chem. C*, 2016, **120**, 11006–11013.
118 J.-S. Li, Y.-J. Tang, C.-H. Liu, S.-L. Li, R.-H. Li, L.-Z. Dong, Z.-H. Dai, J.-C. Bao and Y.-Q. Lan, *J. Mater. Chem. A*, 2016, **4**, 1202–1207.
119 J. Wang, K. Li, H. X. Zhong, D. Xu, Z. L. Wang, Z. Jiang, Z. J. Wu and X. B. Zhang, *Angew. Chem., Int. Ed.*, 2015, **54**, 10530–10534.
120 T. Y. Ma, J. L. Cao, M. Jaroniec and S. Z. Qiao, *Angew. Chem., Int. Ed.*, 2016, **55**, 1138–1142.
121 W. Zhou, T. Xiong, C. Shi, J. Zhou, K. Zhou, N. Zhu, L. Li, Z. Tang and S. Chen, *Angew. Chem., Int. Ed.*, 2016, **55**, 8416–8420.
122 Y. Zheng, Y. Jiao, Y. Zhu, Q. Cai, A. Vasileff, L. H. Li, Y. Han, Y. Chen and S. Z. Qiao, *J. Am. Chem. Soc.*, 2017, **139**, 3336–3339.
123 Y. Zhao, K. Kamiya, K. Hashimoto and S. Nakanishi, *J. Am. Chem. Soc.*, 2015, **137**, 110–113.
124 J. Zhu, K. Sakaushi, G. Clavel, M. Shalom, M. Antonietti and T.-P. Fellinger, *J. Am. Chem. Soc.*, 2015, **137**, 5480–5485.
125 A. Morozan, V. Goellner, Y. Nedellec, J. Hannauer and F. Jaouen, *J. Electrochem. Soc.*, 2015, **162**, H719–H726.
126 N. Cheng, S. Stambula, D. Wang, M. N. Banis, J. Liu, A. Riese, B. Xiao, R. Li, T. K. Sham, L. M. Liu, G. A. Botton and X. Sun, *Nat. Commun.*, 2016, **7**, 13638.
127 J. Deng, P. Ren, D. Deng and X. Bao, *Angew. Chem., Int. Ed.*, 2015, **54**, 2100–2104.
128 X. Cui, P. Ren, D. Deng, J. Deng and X. Bao, *Energy Environ. Sci.*, 2016, **9**, 123–129.
129 J. Zhu, M. Xiao, Y. Zhang, Z. Jin, Z. Peng, C. Liu, S. Chen, J. Ge and W. Xing, *ACS Catal.*, 2016, **6**, 6335–6342.
130 Y. Yang, Z. Lun, G. Xia, F. Zheng, M. He and Q. Chen, *Energy Environ. Sci.*, 2015, **8**, 3563–3571.
131 S. H. Noh, M. H. Seo, J. Kang, T. Okajima, B. Han and T. Ohsaka, *NPG Asia Mater.*, 2016, **8**, e312.
132 P. Cai, S. Ci, E. Zhang, P. Shao, C. Cao and Z. Wen, *Electrochim. Acta*, 2016, **220**, 354–362.
133 T. Wang, Y. Guo, Z. Zhou, X. Chang, J. Zheng and X. Li, *ACS Nano*, 2016, **10**, 10397–10403.
134 Y. Yang, Z. Lin, S. Gao, J. Su, Z. Lun, G. Xia, J. Chen, R. Zhang and Q. Chen, *ACS Catal.*, 2017, **7**, 469–479.
135 J. Chen, G. Xia, P. Jiang, Y. Yang, R. Li, R. Shi, J. Su and Q. Chen, *ACS Appl. Mater. Interfaces*, 2016, **8**, 13378–13383.